FERMILAB-PUB-01/298-E
EFI-2001-45

Search for New Physics in Photon-Lepton Events in $p\bar{p}$ Collisions at $\sqrt{s} = 1.8$ TeV

D. Acosta,[12] T. Affolder,[23] H. Akimoto,[45] A. Akopian,[37] M. G. Albrow,[11] P. Amaral,[8] D. Amidei,[25] K. Anikeev,[24] J. Antos,[1] G. Apollinari,[11] T. Arisawa,[45] A. Artikov,[9] T. Asakawa,[43] W. Ashmanskas,[8] F. Azfar,[30] P. Azzi-Bacchetta,[31] N. Bacchetta,[31] H. Bachacou,[23] S. Bailey,[16] P. de Barbaro,[36] A. Barbaro-Galtieri,[23] V. E. Barnes,[35] B. A. Barnett,[19] S. Baroiant,[5] M. Barone,[13] G. Bauer,[24] F. Bedeschi,[33] S. Belforte,[42] W. H. Bell,[15] G. Bellettini,[33] J. Bellinger,[46] D. Benjamin,[10] J. Bensinger,[4] A. Beretvas,[11] J. P. Berge,[11] J. Berryhill,[8] A. Bhatti,[37] M. Binkley,[11] D. Bisello,[31] M. Bishai,[11] R. E. Blair,[2] C. Blocker,[4] K. Bloom,[25] B. Blumenfeld,[19] S. R. Blusk,[36] A. Bocci,[37] A. Bodek,[36] W. Bokhari,[32] G. Bolla,[35] Y. Bonushkin,[6] D. Bortoletto,[35] J. Boudreau,[34] A. Brandl,[27] S. van den Brink,[19] C. Bromberg,[26] M. Brozovic,[10] E. Brubaker,[23] N. Bruner,[27] E. Buckley-Geer,[11] J. Budagov,[9] H. S. Budd,[36] K. Burkett,[16] G. Busetto,[31] A. Byon-Wagner,[11] K. L. Byrum,[2] S. Cabrera,[10] P. Calafiura,[23] M. Campbell,[25] W. Carithers,[23] J. Carlson,[25] D. Carlsmith,[46] W. Caskey,[5] A. Castro,[3] D. Cauz,[42] A. Cerri,[33] A. W. Chan,[1] P. S. Chang,[1] P. T. Chang,[1] J. Chapman,[25] C. Chen,[32] Y. C. Chen,[1] M. -T. Cheng,[1] M. Chertok,[5] G. Chiarelli,[33] I. Chirikov-Zorin,[9] G. Chlachidze,[9] F. Chlebana,[11] L. Christofek,[18] M. L. Chu,[1] Y. S. Chung,[36] C. I. Ciobanu,[28] A. G. Clark,[14] A. P. Colijn,[11] A. Connolly,[23] J. Conway,[38] M. Cordelli,[13] J. Cranshaw,[40] R. Cropp,[41] R. Culbertson,[11] D. Dagenhart,[44] S. D'Auria,[15] F. DeJongh,[11] S. Dell'Agnello,[13] M. Dell'Orso,[33] S. Demers,[37] L. Demortier,[37] M. Deninno,[3] P. F. Derwent,[11] T. Devlin,[38] J. R. Dittmann,[11] A. Dominguez,[23] S. Donati,[33] J. Done,[39] M. D'Onofrio,[33] T. Dorigo,[16] N. Eddy,[18] K. Einsweiler,[23] J. E. Elias,[11] E. Engels, Jr.,[34] R. Erbacher,[11] D. Errede,[18] S. Errede,[18] Q. Fan,[36] H.-C. Fang,[23] R. G. Feild,[47] J. P. Fernandez,[11] C. Ferretti,[33] R. D. Field,[12] I. Fiori,[3] B. Flaugher,[11] G. W. Foster,[11] M. Franklin,[16] H. Frisch,[8] J. Freeman,[11] J. Friedman,[24] Y. Fukui,[22] I. Furic,[24] S. Galeotti,[33] A. Gallas,[16,*] M. Gallinaro,[37] T. Gao,[32] M. Garcia-Sciveres,[23] A. F. Garfinkel,[35] P. Gatti,[31] C. Gay,[47] D. W. Gerdes,[25] P. Giannetti,[33] V. Glagolev,[9] D. Glenzinski,[11] M. Gold,[27] J. Goldstein,[11] I. Gorelov,[27] A. T. Goshaw,[10] Y. Gotra,[34] K. Goulianos,[37] C. Green,[35] G. Grim,[5] P. Gris,[11] L. Groer,[38] C. Grosso-Pilcher,[8] M. Guenther,[35] G. Guillian,[25] J. Guimaraes da Costa,[16] R. M. Haas,[12] C. Haber,[23] S. R. Hahn,[11] C. Hall,[16] T. Handa,[17] R. Handler,[46] W. Hao,[40] F. Happacher,[13] K. Hara,[43] A. D. Hardman,[35] R. M. Harris,[11] F. Hartmann,[20] K. Hatakeyama,[37] J. Hauser,[6] J. Heinrich,[32] A. Heiss,[20] M. Herndon,[19] C. Hill,[5] A. Hocker,[36] K. D. Hoffman,[35] C. Holck,[32] R. Hollebeek,[32] L. Holloway,[18] B. T. Huffman,[30] R. Hughes,[28] J. Huston,[26] J. Huth,[16] H. Ikeda,[43] J. Incandela,[11,†] G. Introzzi,[33] A. Ivanov,[36] J. Iwai,[45] Y. Iwata,[17] E. James,[25] M. Jones,[32] U. Joshi,[11] H. Kambara,[14] T. Kamon,[39] T. Kaneko,[43] K. Karr,[44] S. Kartal,[11] H. Kasha,[47] Y. Kato,[29] T. A. Keaffaber,[35] K. Kelley,[24] M. Kelly,[25] D. Khazins,[10] T. Kikuchi,[43] B. Kilminster,[36] B. J. Kim,[21] D. H. Kim,[21] H. S. Kim,[18] M. J. Kim,[21] S. B. Kim,[21] S. H. Kim,[43] Y. K. Kim,[23] M. Kirby,[10] M. Kirk,[4] L. Kirsch,[4] S. Klimenko,[12] P. Koehn,[28]

K. Kondo,[45] J. Konigsberg,[12] A. Korn,[24] A. Korytov,[12] E. Kovacs,[2] J. Kroll,[32] M. Kruse,[10] S. E. Kuhlmann,[2] K. Kurino,[17] T. Kuwabara,[43] A. T. Laasanen,[35] N. Lai,[8] S. Lami,[37] S. Lammel,[11] J. Lancaster,[10] M. Lancaster,[23] R. Lander,[5] A. Lath,[38] G. Latino,[33] T. LeCompte,[2] A. M. Lee IV,[10] K. Lee,[40] S. Leone,[33] J. D. Lewis,[11] M. Lindgren,[6] T. M. Liss,[18] J. B. Liu,[36] Y. C. Liu,[1] D. O. Litvintsev,[11] O. Lobban,[40] N. Lockyer,[32] J. Loken,[30] M. Loreti,[31] D. Lucchesi,[31] P. Lukens,[11] S. Lusin,[46] L. Lyons,[30] J. Lys,[23] R. Madrak,[16] K. Maeshima,[11] P. Maksimovic,[16] L. Malferrari,[3] M. Mangano,[33] M. Mariotti,[31] G. Martignon,[31] A. Martin,[47] J. A. J. Matthews,[27] J. Mayer,[41] P. Mazzanti,[3] K. S. McFarland,[36] P. McIntyre,[39] E. McKigney,[32] M. Menguzzato,[31] A. Menzione,[33] P. Merkel,[11] C. Mesropian,[37] A. Meyer,[11] T. Miao,[11] R. Miller,[26] J. S. Miller,[25] H. Minato,[43] S. Miscetti,[13] M. Mishina,[22] G. Mitselmakher,[12] Y. Miyazaki,[29] N. Moggi,[3] E. Moore,[27] R. Moore,[25] Y. Morita,[22] T. Moulik,[35] M. Mulhearn,[24] A. Mukherjee,[11] T. Muller,[20] A. Munar,[33] P. Murat,[11] S. Murgia,[26] J. Nachtman,[6] V. Nagaslaev,[40] S. Nahn,[47] H. Nakada,[43] I. Nakano,[17] C. Nelson,[11] T. Nelson,[11] C. Neu,[28] D. Neuberger,[20] C. Newman-Holmes,[11] C.-Y. P. Ngan,[24] H. Niu,[4] L. Nodulman,[2] A. Nomerotski,[12] S. H. Oh,[10] Y. D. Oh,[21] T. Ohmoto,[17] T. Ohsugi,[17] R. Oishi,[43] T. Okusawa,[29] J. Olsen,[46] W. Orejudos,[23] C. Pagliarone,[33] F. Palmonari,[33] R. Paoletti,[33] V. Papadimitriou,[40] D. Partos,[4] J. Patrick,[11] G. Pauletta,[42] M. Paulini,[23,‡] C. Paus,[24] D. Pellett,[5] L. Pescara,[31] T. J. Phillips,[10] G. Piacentino,[33] K. T. Pitts,[18] A. Pompos,[35] L. Pondrom,[46] G. Pope,[34] M. Popovic,[41] F. Prokoshin,[9] J. Proudfoot,[2] F. Ptohos,[13] O. Pukhov,[9] G. Punzi,[33] A. Rakitine,[24] F. Ratnikov,[38] D. Reher,[23] A. Reichold,[30] P. Renton,[30] A. Ribon,[31] W. Riegler,[16] F. Rimondi,[3] L. Ristori,[33] M. Riveline,[41] W. J. Robertson,[10] A. Robinson,[41] T. Rodrigo,[7] S. Rolli,[44] L. Rosenson,[24] R. Roser,[11] R. Rossin,[31] C. Rott,[35] A. Roy,[35] A. Ruiz,[7] A. Safonov,[5] R. St. Denis,[15] W. K. Sakumoto,[36] D. Saltzberg,[6] C. Sanchez,[28] A. Sansoni,[13] L. Santi,[42] H. Sato,[43] P. Savard,[41] A. Savoy-Navarro,[11] P. Schlabach,[11] E. E. Schmidt,[11] M. P. Schmidt,[47] M. Schmitt,[16,*] L. Scodellaro,[31] A. Scott,[6] A. Scribano,[33] S. Segler,[11] S. Seidel,[27] Y. Seiya,[43] A. Semenov,[9] F. Semeria,[3] T. Shah,[24] M. D. Shapiro,[23] P. F. Shepard,[34] T. Shibayama,[43] M. Shimojima,[43] M. Shochet,[8] A. Sidoti,[31] J. Siegrist,[23] A. Sill,[40] P. Sinervo,[41] P. Singh,[18] A. J. Slaughter,[47] K. Sliwa,[44] C. Smith,[19] F. D. Snider,[11] A. Solodsky,[37] J. Spalding,[11] T. Speer,[14] P. Sphicas,[24] F. Spinella,[33] M. Spiropulu,[8] L. Spiegel,[11] J. Steele,[46] A. Stefanini,[33] J. Strologas,[18] F. Strumia,[14] D. Stuart,[11] K. Sumorok,[24] T. Suzuki,[43] T. Takano,[29] R. Takashima,[17] K. Takikawa,[43] P. Tamburello,[10] M. Tanaka,[43] B. Tannenbaum,[6] M. Tecchio,[25] R. Tesarek,[11] P. K. Teng,[1] K. Terashi,[37] S. Tether,[24] A. S. Thompson,[15] R. Thurman-Keup,[2] P. Tipton,[36] S. Tkaczyk,[11] D. Toback,[39] K. Tollefson,[36] A. Tollestrup,[11] D. Tonelli,[33] H. Toyoda,[29] W. Trischuk,[41] J. F. de Troconiz,[16] J. Tseng,[24] D. Tsybychev,[11] N. Turini,[33] F. Ukegawa,[43] T. Vaiciulis,[36] J. Valls,[38] S. Vejcik III,[11] G. Velev,[11] G. Veramendi,[23] R. Vidal,[11] I. Vila,[7] R. Vilar,[7] I. Volobouev,[23] M. von der Mey,[6] D. Vucinic,[24] R. G. Wagner,[2] R. L. Wagner,[11] N. B. Wallace,[38] Z. Wan,[38] C. Wang,[10] M. J. Wang,[1] B. Ward,[15] S. Waschke,[15] T. Watanabe,[43] D. Waters,[30] T. Watts,[38] R. Webb,[39] H. Wenzel,[20] W. C. Wester III,[11] A. B. Wicklund,[2] E. Wicklund,[11] T. Wilkes,[5] H. H. Williams,[32] P. Wilson,[11] B. L. Winer,[28] D. Winn,[25] S. Wolbers,[11] D. Wolinski,[25] J. Wolinski,[26] S. Wolinski,[25] S. Worm,[27] X. Wu,[14] J. Wyss,[33] W. Yao,[23] G. P. Yeh,[11] P. Yeh,[1] J. Yoh,[11] C. Yosef,[26] T. Yoshida,[29] I. Yu,[21] S. Yu,[32] Z. Yu,[47] A. Zanetti,[42] F. Zetti,[23] and S. Zucchelli[3]

(The CDF Collaboration)
[1]*Institute of Physics, Academia Sinica, Taipei, Taiwan 11529, Republic of China*
[2]*Argonne National Laboratory, Argonne, Illinois 60439*
[3]*Istituto Nazionale di Fisica Nucleare, University of Bologna, I-40127 Bologna, Italy*
[4]*Brandeis University, Waltham, Massachusetts 02254*
[5]*University of California at Davis, Davis, California 95616*
[6]*University of California at Los Angeles, Los Angeles, California 90024*
[7]*Instituto de Fisica de Cantabria, CSIC-University of Cantabria, 39005 Santander, Spain*
[8]*Enrico Fermi Institute, University of Chicago, Chicago, Illinois 60637*
[9]*Joint Institute for Nuclear Research, RU-141980 Dubna, Russia*
[10]*Duke University, Durham, North Carolina 27708*
[11]*Fermi National Accelerator Laboratory, Batavia, Illinois 60510*
[12]*University of Florida, Gainesville, Florida 32611*
[13]*Laboratori Nazionali di Frascati, Istituto Nazionale di Fisica Nucleare, I-00044 Frascati, Italy*
[14]*University of Geneva, CH-1211 Geneva 4, Switzerland*
[15]*Glasgow University, Glasgow G12 8QQ, United Kingdom*
[16]*Harvard University, Cambridge, Massachusetts 02138*
[17]*Hiroshima University, Higashi-Hiroshima 724, Japan*
[18]*University of Illinois, Urbana, Illinois 61801*
[19]*The Johns Hopkins University, Baltimore, Maryland 21218*
[20]*Institut für Experimentelle Kernphysik, Universität Karlsruhe, 76128 Karlsruhe, Germany*
[21]*Center for High Energy Physics: Kyungpook National University, Taegu 702-701; Seoul National University, Seoul 151-742; and SungKyunKwan University, Suwon 440-746; Korea*
[22]*High Energy Accelerator Research Organization (KEK), Tsukuba, Ibaraki 305, Japan*
[23]*Ernest Orlando Lawrence Berkeley National Laboratory, Berkeley, California 94720*
[24]*Massachusetts Institute of Technology, Cambridge, Massachusetts 02139*
[25]*University of Michigan, Ann Arbor, Michigan 48109*
[26]*Michigan State University, East Lansing, Michigan 48824*
[27]*University of New Mexico, Albuquerque, New Mexico 87131*
[28]*The Ohio State University, Columbus, Ohio 43210*
[29]*Osaka City University, Osaka 588, Japan*
[30]*University of Oxford, Oxford OX1 3RH, United Kingdom*
[31]*Universita di Padova, Istituto Nazionale di Fisica Nucleare, Sezione di Padova, I-35131 Padova, Italy*
[32]*University of Pennsylvania, Philadelphia, Pennsylvania 19104*
[33]*Istituto Nazionale di Fisica Nucleare, University and Scuola Normale Superiore of Pisa, I-56100 Pisa, Italy*
[34]*University of Pittsburgh, Pittsburgh, Pennsylvania 15260*
[35]*Purdue University, West Lafayette, Indiana 47907*
[36]*University of Rochester, Rochester, New York 14627*
[37]*Rockefeller University, New York, New York 10021*
[38]*Rutgers University, Piscataway, New Jersey 08855*

[39] Texas A&M University, College Station, Texas 77843
[40] Texas Tech University, Lubbock, Texas 79409
[41] Institute of Particle Physics, University of Toronto, Toronto M5S 1A7, Canada
[42] Istituto Nazionale di Fisica Nucleare, University of Trieste/Udine, Italy
[43] University of Tsukuba, Tsukuba, Ibaraki 305, Japan
[44] Tufts University, Medford, Massachusetts 02155
[45] Waseda University, Tokyo 169, Japan
[46] University of Wisconsin, Madison, Wisconsin 53706
[47] Yale University, New Haven, Connecticut 06520
(Dated: October 4, 2001)

Abstract

We present the results of a search in $p\bar{p}$ collisions at $\sqrt{s} = 1.8$ TeV for anomalous production of events containing a photon with large transverse energy and a lepton (e or μ) with large transverse energy, using 86 pb^{-1} of data collected with the Collider Detector at Fermilab during the 1994-95 collider run at the Fermilab Tevatron. The presence of large missing transverse energy ($\not\!\!E_T$), additional photons, or additional leptons in these events is also analyzed. The results are consistent with standard model expectations, with the possible exception of photon-lepton events with large $\not\!\!E_T$, for which the observed total is 16 events and the expected mean total is 7.6 ± 0.7 events.

PACS numbers: 13.85.Rm, 12.60.Jv, 13.85.Qk, 14.80.Ly

*Now at Northwestern University, Evanston, Illinois 60208
†Now at University of California, Santa Barbara, CA 93106
‡Now at Carnegie Mellon University, Pittsburgh, Pennsylvania 15213

I. INTRODUCTION

An important test of the standard model of particle physics [1] (and the extent of its validity) is to measure and understand the properties of the highest-energy particle collisions. The chief predictions of the standard model for these collisions are the numbers and varieties of fundamental particles, i.e., the fermions and gauge bosons of the standard model, that are produced. The observation of an anomalous production rate of any combination of such particles is therefore a clear indication of a new physical process. This paper describes an analysis of the production of a set of combinations involving at least one photon and at least one lepton (e or μ), using 86 pb^{-1} of data from proton-antiproton collisions collected with the Collider Detector at Fermilab (CDF) [2] during the 1994-95 run of the Fermilab Tevatron.

Production of these particular combinations of particles is of interest for several reasons. Events with photons and leptons are potentially related to the puzzling "$ee\gamma\gamma\not\!\!E_T$" event recorded by CDF [3]. A supersymmetric model [4] designed to explain the $ee\gamma\gamma\not\!\!E_T$ event predicts the production of photons from the radiative decay of the $\tilde{\chi}_2^0$ neutralino, and leptons through the decay of charginos, indicating $\ell\gamma\not\!\!E_T$ events as a signal for the production of a chargino-neutralino pair. Other hypothetical, massive particles could subsequently decay to one or more standard model electroweak gauge bosons, one of which could be a photon and the other of which could be a leptonically decaying W or Z^0 boson. In addition, photon-lepton studies complement similarly motivated inclusive searches for new physics in diphoton [5], photon-jet [6], and photon-b-quark events [7].

The scope and strategy of this analysis are meant to reflect the motivating principles. Categories of photon-lepton events are defined *a priori* in a way that characterizes the dif-

ferent possibilities for new physics. For each category, the inclusive event total is compared with standard model expectations, and a few simple kinematic distributions are presented for further examination. The decay products of massive particles are typically isolated from other particles, and possess large transverse momentum and low rapidity. This search is therefore limited to those events with at least one isolated, central ($|\eta| < 1.0$) photon with $E_T > 25$ GeV, and at least one isolated, central electron or muon with $E_T > 25$ GeV. Studying this class of events has the added advantage of highly efficient detection and data acquisition. These photon-lepton candidates are further partitioned by angular separation. Events where exactly one photon and one lepton are detected nearly opposite in azimuth ($\Delta\varphi_{\ell\gamma} > 150°$) are characteristic of a two-particle final state (two-body photon-lepton events), and the remaining photon-lepton events are characteristic of three or more particles in the final state (multi-body photon-lepton events). The inclusive event totals and kinematic properties of each of these two categories are studied. The multi-body photon-lepton events are then further studied for the presence of additional particles: photons, leptons, or the missing transverse energy associated with weakly interacting neutral particles.

Section 2 describes the CDF detector. Section 3 specifies the methods for identifying photons and leptons, and the selection of photon-lepton candidates. Section 4 estimates the standard model sources of photon-lepton candidates in the various search categories. Section 5 compares the standard model expectations with the CDF data. Section 6 presents the conclusions of the analysis.

II. THE CDF DETECTOR

The CDF detector is a cylindrically symmetric, forward-backward symmetric particle detector designed to study $\bar{p}p$ collisions at the Fermilab Tevatron. A schematic drawing of

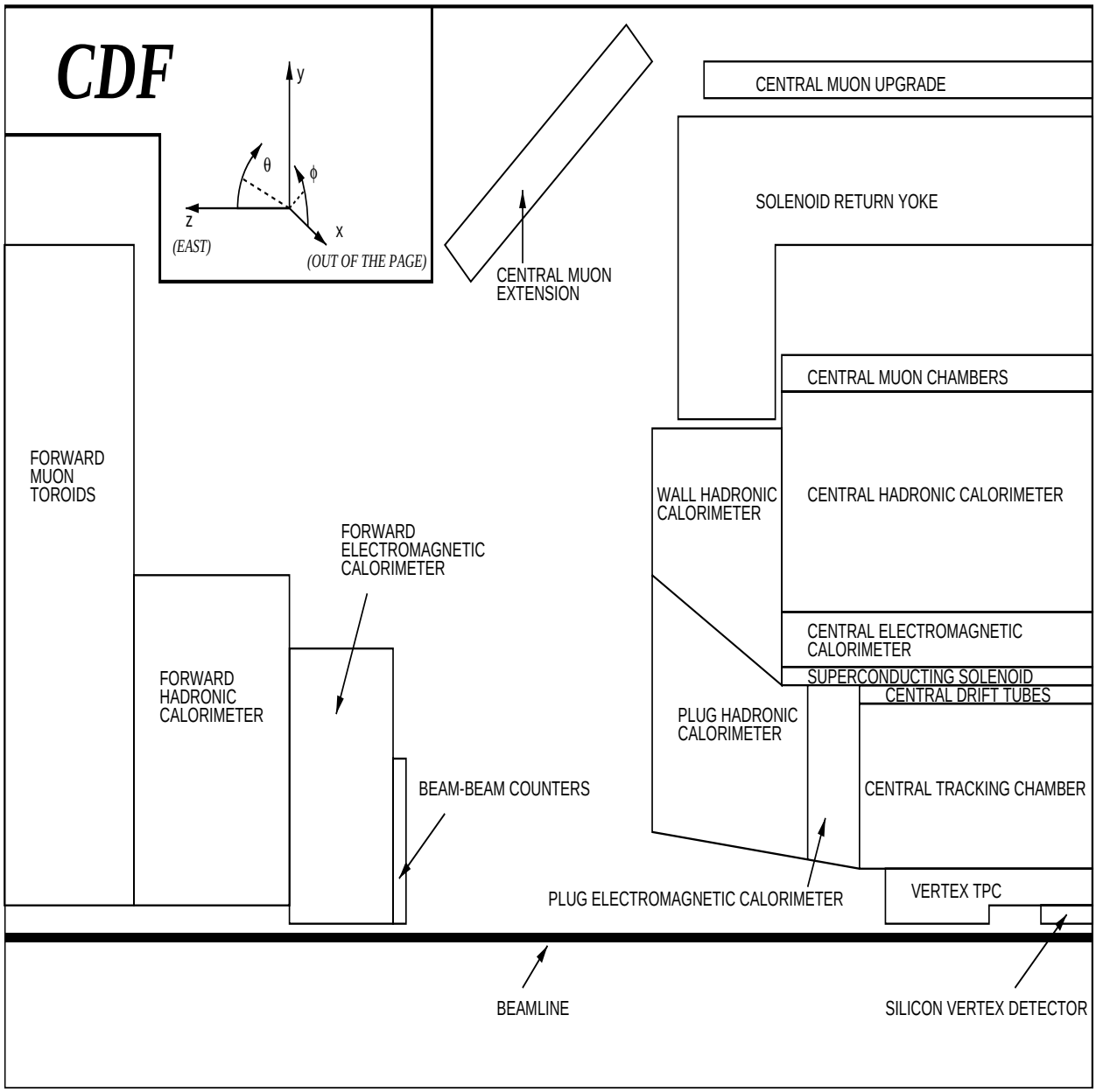

FIG. 1: A schematic drawing of one quadrant of the CDF detector.

the major detector components is shown in Figure 1. A superconducting solenoid of length 4.8 m and radius 1.5 m generates a magnetic field of 1.4 T and contains tracking chambers used to detect charged particles and measure their momenta. Sampling calorimeters, used to measure the electromagnetic and hadronic energy deposited by electrons, photons, and jets of hadrons, surround the solenoid. Outside the calorimeters are drift chambers used for

muon detection. In this section the subsystems relevant to this analysis are briefly described; a more detailed description can be found elsewhere [2].

A set of vertex time projection chambers (VTX) [8] provides measurements in the r-z plane up to a radius of 22 cm and detects particle tracks in the region $|\eta| < 3.25$. VTX tracks are used to find the z position of the $\bar{p}p$ interaction (z_{event}) and to constrain the origin of track helices. The 3.5-m-long central tracking chamber (CTC) is a wire drift chamber which provides up to 84 measurements between the radii of 31.0 cm and 132.5 cm, efficient for track detection in the region $|\eta| < 1.0$. The CTC measures the momenta of charged particles with momentum resolution $\sigma_p/p < \sqrt{(0.0011p)^2 + (0.0066)^2}$, where p is measured in GeV/c.

The calorimeter, segmented into towers projecting to the nominal interaction point, is divided into three separate η regions: a central barrel which surrounds the solenoid coil ($|\eta| < 1.1$), 'end-plugs' ($1.1 < |\eta| < 2.4$), and forward/backward modules ($2.4 < |\eta| < 4.2$). The central barrel has an electromagnetic calorimeter (CEM) which absorbs and measures the total energy of electrons and photons and also a portion of the energies of penetrating hadrons and muons. The CEM is a sampling calorimeter consisting of polystyrene scintillator sandwiched between lead absorber sheets, and is segmented into 480 towers spanning 15° in φ and 0.1 in η. The CEM is also instrumented with proportional chambers (CES) embedded near shower maximum at approximately 6 radiation lengths. Wires and cathode strips in the CES measure electromagnetic shower profiles in the φ and z views, respectively. Beyond the outer radius of the CEM is a hadronic calorimeter (CHA) which absorbs and measures the energy of hadrons and also a portion of the energy of penetrating muons. The CHA is a sampling calorimeter consisting of acrylic scintillator sandwiched between iron absorber sheets, and is segmented similarly to the CEM. An endwall hadronic calorimeter

(WHA) covers the gap between the central barrel calorimeter and the end-plug calorimeters, with construction similar to the CHA. The end-plug calorimeters, one on each side of the central barrel, have an electromagnetic calorimeter (PEM) consisting of proportional chambers sandwiched between lead absorber sheets, and a hadronic calorimeter (PHA) consisting of proportional chambers sandwiched between iron absorber sheets. The PEM and PHA are both segmented into towers spanning 5° in φ and 0.09 in η. The forward/backward modules also have electromagnetic (FEM) and hadronic (FHA) calorimeters, and are constructed similarly to the PEM and PHA.

Muons are detected with three systems of muon chambers situated outside the calorimeters in the region $|\eta| < 1.1$. The central muon detector (CMU) system consists of four layers of drift chambers directly outside the central hadronic calorimeter, covering 84% of the solid angle for $|\eta| < 0.6$. Outside of the CMU system is 0.6 m of steel shielding, followed by the central muon upgrade (CMP) system. The CMP system consists of four layers of drift chambers covering 63% of the solid angle for $|\eta| < 0.6$. About 53% of the solid angle for $|\eta| < 0.6$ is covered by both the CMU and the CMP. The central muon extension (CMX) system consists of eight layers of drift tubes sandwiched between scintillation counters. The CMX detector covers 71% of the solid angle for $0.6 < |\eta| < 1.0$. Figure 2 shows the coverage in η-φ space for the three muon detection systems. In each muon system the drift chambers reconstruct the position of charged particles using the time-to-distance relationship in the transverse (r-φ) plane, and charge division in the longitudinal (r-z) plane. Three-dimensional muon track segments ("muon stubs") consist of position measurements in at least three layers of chambers, in both the r-φ and r-z planes.

A three-level multipurpose trigger is used to select $p\bar{p}$ collisions for analysis. Each level is a logical `OR` of a number of triggers designed to select events with electrons, muons, photons,

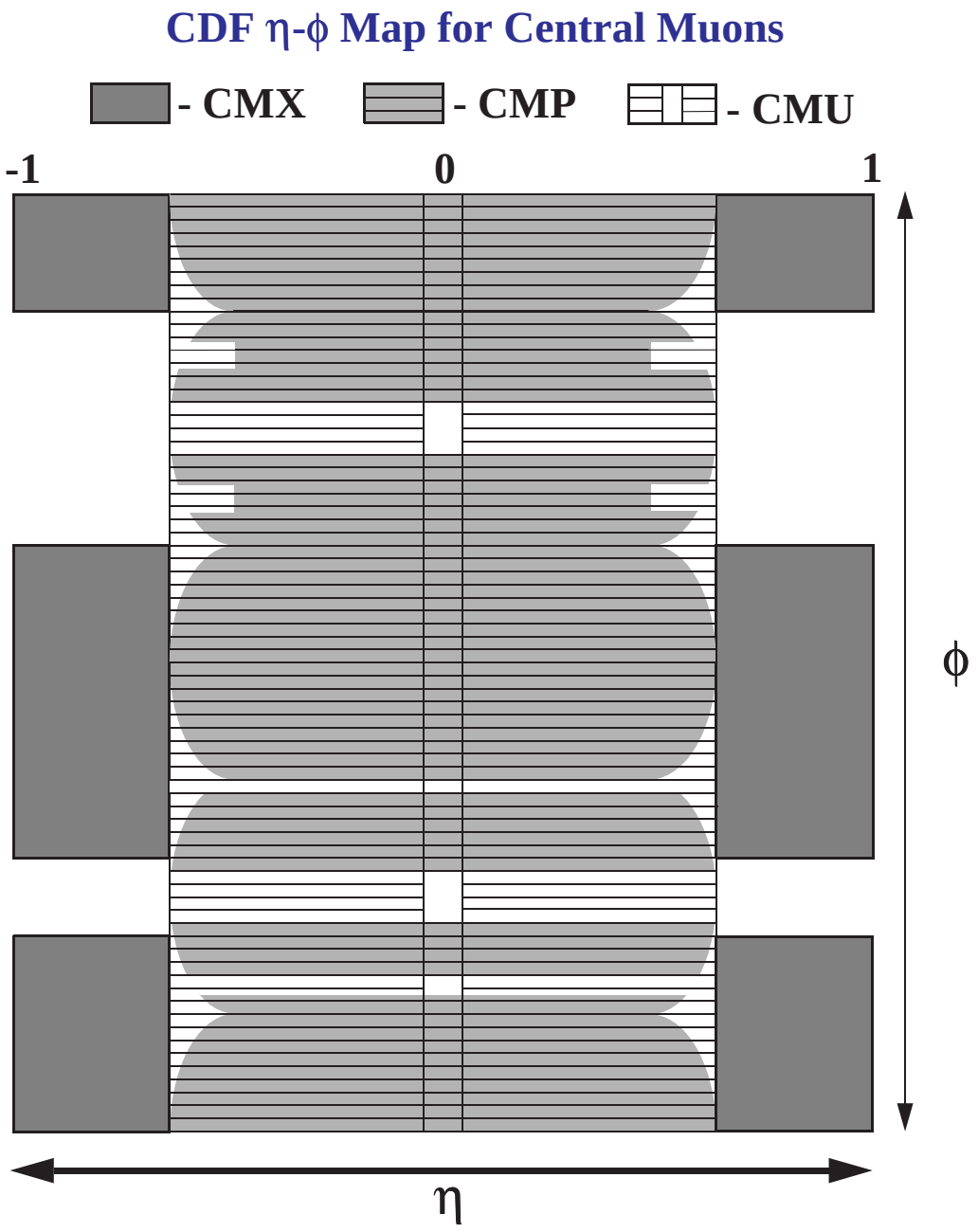

FIG. 2: The coverage in η-φ space of the CDF central muon systems for the 1994-95 run [9].

or jets. The function of each trigger level is briefly described here; the particular trigger combinations employed in this analysis are specified in Section III.

The first trigger stage, "Level 1", uses fast outputs from the three central muon detectors for muon triggers, and fast outputs from all the calorimeters for electron and jet triggers.

The second trigger stage, "Level 2", combines tracking data and clusters of energy in the calorimeters to form muon, electron, photon, and jet candidates. A list of calorimeter clusters is provided by a nearest-neighbor hardware cluster finder. For each cluster, the E_T, average φ, and average η are determined. Jet candidates are selected from this list of clusters, and clusters that predominantly consist of electromagnetic calorimeter energy are identified as electron or photon candidates. A list of r-φ tracks is provided by the central fast tracker (CFT) [10], a hardware track processor, which uses fast timing information from the CTC as input. A list of muon stubs is obtained from the central muon detectors, and they are matched to CFT tracks to form muon candidates. CFT tracks can also be matched to electromagnetic energy clusters to form electron candidates. A decision by the Level 2 hardware to accept the event initiates full readout of the CDF detector data. The last trigger stage, "Level 3", performs full event reconstruction using software executed by commercial processors. Electron, muon, photon, and jet candidates are selected using algorithms similar to those employed in the final offline analysis, and a final trigger decision selects events to be recorded for later analysis.

III. SELECTION OF PHOTON-LEPTON CANDIDATES

Photon-lepton candidates are obtained from three different samples of events selected by the Level 3 trigger: inclusive photon events and inclusive muon events, from which photon-muon candidates are selected; and inclusive electron events, from which photon-electron candidates are selected. The methods for lepton identification [11] and photon identification [3, 7] are very similar to those of previous analyses. The offline identification requirements of photons and the selection of photon-muon candidates from the inclusive photon sample are described in Section III A; the offline identification requirements of muons

and the selection of photon-muon candidates from a muon trigger sample are described in Section III B. The offline identification requirements of electrons and the selection of photon-electron candidates are described in Section III C. The identification requirements of missing transverse energy, additional photons, or additional leptons in the photon-lepton sample are described in Section III D. A description of the subsamples of photon-lepton candidates to be analyzed is given in Section III E.

All CDF data samples described in this paper satisfy the following requirements: $|z_{event}|$ is less than 60 cm, so that the collision is well-contained by the CDF detector; and there is no measurable energy in the calorimeters recorded out of time (more than 20 ns early or more than 35 ns late, as measured by TDC's within the CHA) with the $p\bar{p}$ collision time, in order to suppress cosmic ray events and backgrounds related to the Main Ring accelerator.

A. Photon Identification

Photon selection criteria are listed in Table I and are described below. For the energies considered here, the response of the CEM to photons is nearly identical to that of electrons; the reconstruction and identification of electrons and photons are therefore very similar, the chief difference being the high momentum track left by the former and the absence of any tracks left by the latter. Photon or electron candidates in the CEM are chosen from clusters of energy in adjacent CEM towers. A cluster starts from seed towers exceeding 3 GeV in energy, and spans three towers in η by one tower in φ, with no sharing of towers between different clusters. The total photon or electron energy is the sum of the energies of the towers in a cluster, where the energy scales of the CEM towers are calibrated by electrons

from Z^0 decays. The energy resolution of a CEM electron or photon is given by [12]

$$\left(\frac{\delta E}{E}\right)^2 = \left(\frac{(13.5 \pm 0.7)\%\ \mathrm{GeV}^{1/2}}{\sqrt{E_T}}\right)^2 + (1.5 \pm 0.3\%)^2. \quad (1)$$

The resolution for $E_T > 25$ GeV is better than 3%.

For photons or electrons, the CES shower position is determined by the energy-weighted centroid of the highest energy clusters of those strips and wires in the CES corresponding to the seed tower of the CEM energy cluster. For electrons, the shower position is determined by the clusters of strips and wires in the CES closest to the position of the electron track, when the track is extrapolated to the CES radius. Similarly, the photon direction is determined by the line connecting the primary event vertex to the CES shower position, and the electron direction is determined by the electron track.

Photon candidates	
CEM fiducial photon	
Photon E_T	> 25 GeV
Tracks with $p_T > 1$ GeV/c	$= 0$
Tracks with $p_T \leq 1$ GeV/c	≤ 1
E_{HAD}/E_{EM}	$< 0.055 + 0.00045\ \mathrm{GeV}^{-1} \times E^{\gamma}$
$\chi^2_{avg} = (\chi^2_{strip} + \chi^2_{wire})/2$	< 20
E^{CES}_{2nd}	$< 2.39\ \mathrm{GeV} + 0.01 \times E^{\gamma}$
E_T in a cone of 0.4, E^{iso}_{cone}	< 2 GeV
p_T of tracks in a cone of 0.4	< 5 GeV/c

TABLE I: The selection criteria used to identify photon candidates.

To ensure that events are well measured, the shower positions of electron or photon candidates are required to fall within the fiducial volume of the CEM. To be in the fiducial region, the shower position is required to lie within 21 cm of the tower center in the r-φ view so that the shower is fully contained in the active region. The region $|\eta| < 0.05$, where the two halves of the detector meet, is excluded. The region $0.77 < \eta < 1.0, 75^\circ < \varphi < 90^\circ$ is

uninstrumented because it is the penetration for the cryogenic connections to the solenoidal magnet. In addition, the region $1.0 < |\eta| < 1.1$ is excluded because of the smaller depth of the electromagnetic calorimeter in that region. The fiducial CEM coverage per photon or electron is 81% of the solid angle in the region defined by $|\eta| < 1.0$.

Inclusive photon trigger	
CEM photon	
E_T	> 23 GeV
Fiducial CES cluster	
$E_{3x3}^{iso} < 4$ GeV OR $E_T > 50$ GeV	
Inclusive muon trigger	
CMNP, CMUP, or CMX muon	
p_T	> 18 GeV/c
CHA energy	< 6 GeV
Track-stub matching:	
$\lvert\Delta x_{stub}\rvert$	< 5 cm (CMNP, CMUP)
$\lvert\Delta x_{stub}\rvert$	< 10 cm (CMX)
Inclusive electron trigger	
CEM electron	
E_T	> 18 GeV
p_T	> 13 GeV/c
E_{HAD}/E_{EM}	< 0.125
χ^2_{strip}	< 10
L_{shr}	< 0.2
Track-CES matching:	
$\lvert\Delta x_{CES}\rvert$	< 3 cm
$\lvert\Delta z_{CES}\rvert$	< 5 cm

TABLE II: Level 3 trigger criteria for the inclusive photon, inclusive muon, and inclusive electron samples.

Photon candidates are required to have tracking and CEM shower characteristics consistent with that of a single, neutral, electromagnetically interacting particle. No CTC tracks with $p_T > 1$ GeV/c may point at the CEM towers in the photon cluster; at most one

track with $p_T < 1$ GeV/c is allowed to point at these same towers. The ratio, E_{HAD}/E_{EM}, of the total energy E_{HAD} of the CHA towers located behind the CEM towers in the photon cluster to the total energy E_{EM} of those CEM towers, is required to be less than $0.055 + 0.00045\ \mathrm{GeV}^{-1} \times E^{\gamma}$, where E^{γ} is the energy of the photon candidate. A χ^2 statistic is used to compare the energy deposited in the CES wires (χ^2_{wire}) and cathode strips (χ^2_{strip}) to that expected from test beam data. The average of the two measurements, χ^2_{avg}, is required to be less than 20. The CES cluster of second highest energy in the CEM seed tower, E^{CES}_{2nd}, is required to be less than $2.39 + 0.01 \times E^{\gamma}$ in units of GeV. The last two requirements suppress CEM clusters arising from hadrons, since hadron decay typically results in two or more closely spaced photons.

Calorimeter and tracking data in a cone of η-φ space, defined by a radius of $R \equiv \sqrt{\Delta\eta^2 + \Delta\varphi^2} < 0.4$ surrounding the photon cluster, are used to discriminate photons produced in isolation from those originating in jets of hadrons. The total transverse energy deposited in the calorimeters in a cone of $R = 0.4$ around the photon shower position is summed, and the photon E_T is subtracted. If there are multiple $p\bar{p}$ interactions in the event, the mean transverse energy in a cone of $R = 0.4$ per additional interaction (0.23 GeV/interaction) is also subtracted. The mean transverse energy leakage of the photon shower into CEM towers outside the photon cluster, as a function of photon shower position, is also subtracted. The remaining energy in the cone is the photon isolation energy, E^{iso}_{cone}, which is required to be less than 2 GeV. As an additional indicator of photon isolation, the sum of the momenta of CTC tracks incident upon a cone of $R = 0.4$ around the photon shower position must be less than 5 GeV/c.

An inclusive photon sample is selected with the CDF trigger requirements described below and summarized in Table II. At Level 1, events are required to have at least one CEM trigger

tower [13] with E_T exceeding 8 GeV. At Level 2, a low-threshold, isolated photon trigger selects events with CEM clusters exceeding 23 GeV in E_T (computed assuming $z_{event} = 0.0$). In addition, a CES energy cluster is required to accompany the CEM cluster, and the additional transverse energy deposited in an array of calorimeter towers spanning three towers in η by three towers in φ surrounding the CEM cluster, E_{3x3}^{iso}, is required to be less than approximately 4 GeV. Alternatively at Level 2, a high-threshold photon trigger selects events with CEM clusters exceeding 50 GeV in E_T. At Level 3, the full offline CEM clustering is performed and events passing the low-threshold isolated photon trigger are required to have fiducial CEM clusters with $E_T > 23$ GeV; events passing the high-threshold photon trigger are required to have fiducial CEM clusters with $E_T > 50$ GeV. Events selected by these photon triggers are then required to have at least one photon candidate, satisfying all offline photon selection requirements, with 25 GeV $< E_T <$ 55 GeV for events passing the low-threshold trigger, or with $E_T \geq 55$ GeV for events passing the high-threshold trigger. This results in an inclusive photon sample of 314,420 events. The trigger efficiency for the low-threshold trigger increases from 43% to 89% as photon E_T increases from 25 GeV to 31 GeV, and remains constant at 89% from 31 GeV to 55 GeV. The trigger efficiency for the high-threshold trigger is greater than 99%. The detection efficiency of the offline photon selection criteria is $86.0 \pm 0.7\%$ [14].

Photon-muon candidate events are selected from the inclusive photon sample by requiring at least one muon in addition to the photon in the event. The muon can have any of the central muon stub types described in Section III B, the muon track must have $p_T >$ 25 GeV/c, and all of the offline muon selection requirements must be satisfied, as described in Section III B and summarized in Table III. This results in a photon-muon sample of 28 events.

Electron candidates	
CEM fiducial electron	
Electron E_T	> 25 GeV
$p_T \times c$	$> 5/9 \times E_T$
Track-CES matching:	
$\quad \lvert\Delta x_{CES}\rvert$	< 1.5 cm
$\quad \lvert\Delta z_{CES}\rvert$	< 3 cm
Track-vertex matching:	
$\quad \lvert\Delta z_{event}\rvert$	< 5 cm
E_{HAD}/E_{EM}	< 0.05
χ^2_{strip}	< 10
$\lvert L_{shr}\rvert$	< 0.2
Photon conversion removal	
Isolation E_T	$< 0.1 \times E_T$
Muon candidates	
CMNP, CMUP, CMX, CMP, or CMU muon	
Track p_T	> 25 GeV/c
Track-stub matching:	
$\quad \lvert\Delta x_{stub}\rvert$	< 5 cm (CMP, CMX)
$\quad \lvert\Delta x_{stub}\rvert$	< 2 cm (all other)
Track-vertex matching:	
$\quad \lvert d_0\rvert$	< 0.3 cm
$\quad \lvert\Delta z_{event}\rvert$	< 5 cm
CEM energy	< 2 GeV
CHA energy	< 6 GeV
CEM+CHA energy	> 0.1 GeV
Isolation E_T	$< 0.1c \times p_T$

TABLE III: The selection criteria used to identify electron and muon candidates.

B. Muon Identification

Muons are identified by extrapolating CTC tracks through the calorimeters, and the extrapolation must match to a stub in either the CMU, CMP, or CMX. There are five different types of track-stub matches: tracks which intersect only the CMU and match a

CMU stub (CMNP muons), tracks which intersect both the CMU and CMP and match stubs in both (CMUP muons), tracks which intersect both the CMU and CMP and match a stub in the CMU only (CMU muons), tracks which intersect the CMP and match a stub in the CMP only (CMP muons), and tracks which intersect the CMX and match a stub in the CMX (CMX muons). For offline identification, CMP and CMX muons are required to have a matching distance (Δx_{stub}) less than 5 cm, and all other muon types are required to have a matching distance less than 2 cm. CTC tracks that are matched to muon stubs are required to be well-measured and to be consistent with originating from the primary event vertex. The muon track is required to have a minimum of six layers of CTC wire measurements, at least three of which must be axial wire measurements and at least two of which must be stereo wire measurements. The distance of closest approach of the CTC track to the primary event vertex must be less than 3 mm in the r-φ view (d_0), and less than 5 cm in the z direction (Δz_{event}). Muon tracks which match with z_{event} are refit with the additional constraint of originating from the primary event vertex ("beam-constrained"), which improves muon momentum resolution by a factor of approximately two. The curvature resolution for beam-constrained muons satisfying all offline selection requirements is given by

$$\delta(1/p_T) \;=\; (0.091 \pm 0.004) \times 10^{-2} (\mathrm{GeV}/c)^{-1}, \tag{2}$$

corresponding to a p_T resolution of 2–8% for muons with p_T ranging from 25–100 GeV/c [12].

High energy muons are typically isolated, minimum-ionizing particles which have limited calorimeter activity. A muon traversing the CEM deposits an average energy of 0.3 GeV; muon candidates are therefore required to deposit less than 2 GeV total in the CEM tower(s) the muon track intersects. Similarly, muons traversing the CHA deposit an average energy of 2 GeV, and so muon candidates are required to deposit less than 6 GeV total in the

intersecting CHA tower(s). An additional requirement that the sum of all energies in the intersecting CEM and CHA towers exceeds 0.1 GeV is imposed in order to suppress hadrons or cosmic rays which may have passed through cracks in the central calorimeters. Finally, in order to further suppress hadrons and muons arising from the decay of hadrons, the total transverse energy deposited in the calorimeters, in a cone of $R = 0.4$ around the muon track direction, must be less than 0.1 times the muon track transverse momentum in GeV/c. The detection efficiency of the offline muon selection criteria is $93.0 \pm 0.3\%$ [15].

Photon-muon candidates are obtained from CDF muon triggers as follows. At Level 1, a muon stub is required in either the CMU or CMX. Muon p_T is inferred from the angle of incidence of the muon stub due to deflection by the magnetic field of the solenoid; CMU stub p_T must exceed 6 GeV/c, and CMX stub p_T must exceed 10 GeV/c. In addition, a minimum energy of 300 MeV is required in the CHA tower associated with the muon stub. At Level 2, a CFT track with $p_T > 12$ GeV/c is required to point within 5° of a CMUP, CMNP, or CMX muon stub triggered at Level 1. Level 2 inclusive muon triggers are prescaled due to bandwidth limitations; more restrictive (but not prescaled) triggers at Level 2 must be employed to increase the selection efficiency for photon-muon candidates. To this end, a Level 2 trigger with no prescaling selects events which pass the Level 2 muon trigger requirements and which also have a calorimeter energy cluster with Level 2 cluster $E_T > 15$ GeV. At Level 3, as summarized in Table II, a fully reconstructed CMUP, CMNP, or CMX muon is required, with maximum track-stub matching distances of 5 cm, 5 cm, and 10 cm, respectively. The muon track p_T must exceed 18 GeV/c, and the energy deposited in a CHA tower by the muon must be less than 6 GeV. Photon-muon candidates are selected from 313,963 events passing the Level 3 muon triggers by requiring at least one CMUP, CMNP, or CMX muon candidate satisfying all offline muon selection requirements,

as described in Table III, and at least one photon candidate satisfying all offline photon selection requirements, as described in Table I. This results in a photon-muon sample of 20 events. When combined with the 28 photon-muon events from the photon triggers in Section III A, a sample of 29 unique photon-muon events is obtained. Of those 29 events, 9 events satisfied only the photon trigger requirements, 1 event satisfied only the muon trigger requirements, and 19 events satisfied both the photon and muon trigger requirements.

The efficiency for CMUP photon-muon or CMNP photon-muon candidates is $84 \pm 3\%$; the efficiency for CMX photon-muon candidates is $68 \pm 5\%$ [14]. When photon-muon candidates from the muon triggers are combined with those from the photon triggers in Section III A, the combined trigger efficiency varies with photon E_T and muon stub type, with an average efficiency exceeding 90%.

C. Electron Identification

Electrons are identified in the CEM by matching high momentum CTC tracks to high energy CEM clusters, as summarized in Table III. The track of highest p_T which intersects one of the towers in a CEM cluster is defined to be the electron track. An electron candidate is required to have a track with p_T (in GeV/c) $>$ 5/9 of the CEM cluster E_T (in GeV). The track position, as extrapolated to the CES radius, is required to fall within 1.5 cm of the CES shower position of the cluster in the r-φ view (Δx_{CES}), and within 3 cm of the CES shower position in the z direction (Δz_{CES}). The distance of closest approach of the CTC track to the primary event vertex must be less than 5 cm in the z direction (Δz_{event}).

The CEM shower characteristics of electron candidates must be consistent with that of a single charged particle. The ratio, E_{HAD}/E_{EM}, of the total energy of the CHA towers located behind the CEM towers in the electron cluster to that of the electron itself is required

to be less than 0.05. A statistic comparing the energy deposited in the CES cathode strips to that expected from test beam data, χ^2_{strip}, is required to be less than 10. A comparison of the lateral shower profile in the CEM cluster with test beam data is parameterized by a dimensionless quantity, L_{shr}, which is required to have a magnitude less than 0.2 [16]. Electrons from photon conversions are removed using an algorithm based on tracking information [11]. Finally, as an additional isolation requirement, the total transverse energy deposited in the calorimeters, in a cone of $R = 0.4$ around the electron track, must be less than 10% of the electron E_T. The detection efficiency of the offline electron selection criteria is $81.0 \pm 0.2\%$ [15].

Photon-electron candidates are obtained from a CDF electron trigger as follows. At Level 1, events are required to have at least one CEM trigger tower [13] with E_T exceeding 8 GeV. At Level 2, two CEM clusters with $E_T > 16$ GeV are required, and also the ratio E_{HAD}/E_{EM} of each cluster is required to be less than 0.125. The Level 3 electron trigger, summarized in Table II, requires a CEM cluster with $E_T > 18$ GeV matched to a CTC track with $p_T > 13$ GeV/c. In addition, a set of electron identification criteria less selective than offline identification criteria is imposed: E_{HAD}/E_{EM} is required to be less than 0.125, the CES cathode strip χ^2 is required to be less than 10, the magnitude of L_{shr} is required to be less than 0.2, and the electron track must match the CES position by 3 cm in Δx_{CES} and by 5 cm in Δz_{CES}.

Photon-electron candidates are selected from 474,912 events passing the Level 3 electron trigger by requiring at least one electron candidate satisfying all offline electron selection requirements, as described in Table III, and at least one photon candidate satisfying all offline photon selection requirements, as described in Table I. This results in a photon-electron sample of 48 events. The efficiency of the CDF electron trigger requirements for

photon-electron candidates is $98.5 \pm 1.5\%$ [14].

D. Selection of Additional Objects

In addition to inclusive photon-lepton production, this analysis investigates the associated production of other photons, other leptons, and large missing transverse energy. Identification of additional photon candidates is the same as that described in Section III A and summarized in Table I. The identification of additional leptons is less selective, because the presence of the primary photon and lepton provides good trigger efficiency and reduces the sources of misidentified particles.

The selection of additional electron candidates is identical to that of previous CDF analyses [16] and is summarized in Table IV. Additional electron candidates in the CEM ("LCEM electrons") are identified with criteria similar to, but looser than that of the primary electron candidates in Section III C: electron E_T must be 20 GeV or greater; electron track p_T (in GeV/c) must exceed half of the electron E_T (in GeV); the ratio E_{HAD}/E_{EM} for the electron must be less than 0.1; and the total transverse energy deposited in the calorimeters, in a cone of $R = 0.4$ around the electron direction, must be less than 10% of the electron E_T. The detection efficiency of these electron selection criteria is $88.9 \pm 0.4\%$ for candidates with $E_T > 20$ GeV.

Additional electron identification is extended to the endplug and forward regions of the calorimeter. Electron candidates originate with clusters of energy in the PEM or FEM with cluster E_T in excess of 15 GeV and 10 GeV, respectively. For PEM electrons, a statistic comparing the energy deposited in a 3×3 array of PEM towers surrounding the PEM cluster to that expected from test beam data, $\chi^2_{3\times3}$, is required to be less than 3. The ratio E_{HAD}/E_{EM} of the total energy of the PHA (FHA) towers located behind the PEM (FEM)

LCEM electron	
E_T	> 20 GeV
$p_T \times c$	$> 1/2 \times E_T$
E_{HAD}/E_{EM}	< 0.1
Isolation E_T	$< 0.1 \times E_T$
PEM electron	
E_T	> 15 GeV
E_{HAD}/E_{EM}	< 0.1
$\chi^2_{3\times3}$	< 3.0
Isolation E_T	$< 0.1 \times E_T$
FEM electron	
E_T	> 10 GeV
E_{HAD}/E_{EM}	< 0.1
Isolation E_T	$< 0.1 \times E_T$
CMI muon	
p_T	> 20 GeV/c
$\lvert\eta_\mu\rvert$	< 1.2
Track-vertex matching:	
$\lvert d_0\rvert$	< 0.3 cm
$\lvert\Delta z_{event}\rvert$	< 5 cm
CEM energy	< 2 GeV
CHA energy	< 6 GeV
CEM+CHA energy	> 0.1 GeV
p_T of tracks in a cone of 0.4	$< 0.1 \times p_T$
Isolation E_T	$< 0.1c \times p_T$

TABLE IV: The selection criteria used to identify additional lepton candidates.

towers in the electron cluster to that of the electron itself, is required to be less than 0.1. As an isolation requirement, the total transverse energy deposited in the calorimeters, in a cone of $R = 0.4$ around the cluster direction, must be less than 10% of the cluster E_T. The detection efficiency of these selection criteria is $87.4 \pm 0.7\%$ for PEM electrons with $E_T > 15$ GeV and $75.4 \pm 2.6\%$ for FEM electrons with $E_T > 10$ GeV.

Additional muon candidates include the following: any muon satisfying the criteria in Table III, with the muon p_T requirement lowered to 20 GeV/c; or an isolated CTC track consistent with that of a minimum ionizing particle (CMI muons), the criteria for which are summarized in Table IV. CTC tracks in the central region of the detector ($|\eta_\mu| < 1.2$) which do not extrapolate to any of the central muon chambers are required to have beam-constrained $p_T > 20$ GeV/c, and are required to satisfy all of the muon selection requirements in Section III B, with the following exceptions: the muon stub matching requirement is no longer employed; and the isolation requirements are supplemented by the requirement that the sum of the momenta of CTC tracks, incident upon a cone of $R = 0.4$ around the muon track, be less than 0.1 of the muon track p_T. The detection efficiency of these selection criteria is $91.3 \pm 1.3\%$ for CMI muons with $p_T > 20$ GeV/c.

The missing transverse energy of an event, $\not\!\!E_T$, is calculated as follows. For each tower of each calorimeter, a vector $\vec{E}_T^{\,i}$ is defined whose magnitude equals the calorimeter transverse energy, as determined by the line directed from the primary event vertex to the calorimeter tower center, and whose direction is that of the same line projected into the plane transverse to the beam direction. The opposite of the vector sum over all calorimeter towers,

$$\vec{\not\!\!E}_T(raw) \;=\; -\sum_i \vec{E}_T^{\,i}, \tag{3}$$

is a first approximation of $\not\!\!E_T$. In this paper, the measurement of $\not\!\!E_T$ is improved by the identification of jets, muons, electrons, and photons, as described below.

Jets of hadrons are identified via clusters of energy measured by the calorimeters. A jet reconstruction algorithm [17] finds clusters of energy deposited in cones of fixed radius $R = 0.4$. The jet energy and jet direction are measured using the total energy and the energy-weighted centroid, respectively, of the calorimeter towers contained in the cone. The jet energy is then corrected for non-linearity in the response of the calorimeters, the leakage

of energy between calorimeter towers, the energy deposited outside of the jet cone, the energy from the underlying $p\bar{p}$ collision debris, and the energy from any additional $p\bar{p}$ interactions. These corrections result in mean increases of 70% (35%) to the raw jet E_T, for jets with raw E_T of 10 GeV (100 GeV) [11].

An estimate of $\not\!\!E_T$ which takes into account the corrected jet energies, $\not\!\!E_T(j)$, is obtained from $\not\!\!E_T(raw)$ by adding for each jet the raw jet momentum vector, $\vec{E}_T^j(raw)$, and subtracting the corrected jet momentum vector, $\vec{E}_T^j(cor)$:

$$\vec{\not\!\!E}_T(j) \;=\; \vec{\not\!\!E}_T(raw) - \sum_j \left(1 - \frac{E_T^j(raw)}{E_T^j(cor)}\right)\vec{E}_T^j(cor). \qquad (4)$$

The jets included in this sum are required to have $E_T^j(raw) > 8$ GeV and $|\eta_j| < 2.4$.

Muons penetrate the calorimeters, so their energy is not accounted for in $\not\!\!E_T(raw)$ and must be included separately. Muons with any combination of stubs in the central muon chambers are included in the $\not\!\!E_T$ calculation, provided that the beam-constrained muon track p_T exceeds 10 GeV/c, less than 6 GeV of energy is deposited in intersecting CHA towers, less than 2 GeV of energy is deposited in intersecting CEM towers, and Δx_{stub} satisfies the requirements in Table III. High momentum tracks without matching muon chamber stubs are also included, provided that all of the CMI muon criteria in Table IV are satisfied, except for the following differences: the track need not extrapolate to regions uninstrumented by muon chambers; the isolation requirements in Table IV are rescinded; and in their place is added the requirement that the total transverse energy deposited in the calorimeters, in a cone of $R = 0.4$ around the track direction, must be less than 5 GeV. An estimate of $\not\!\!E_T$ which takes into account the muons described above, $\not\!\!E_T(j\mu)$, is obtained from $\not\!\!E_T(j)$ by subtracting for each muon the muon momentum vector, $\vec{p}_T^{\,\mu}$, and adding the transverse energy vector, $\vec{E}_T^{\mu}$, of the total energy deposited in intersecting CHA and CEM

towers:

$$\vec{\not\!\!E}_T(j\mu) \;=\; \vec{\not\!\!E}_T(j) - \sum_{\mu}\left(1 - \frac{E_T^{\mu}}{cp_T^{\mu}}\right)c\vec{p}_T^{\,\mu}. \tag{5}$$

The response of the calorimeters to high energy electrons and photons differs from that of jets of hadrons, so their energy is not properly accounted for by $\not\!\!E_T(j\mu)$. The following types of electrons and photons are included in this correction: any CEM photon satisfying the criteria in Table I; and any CEM, PEM, or FEM electron satisfying criteria identical to that listed in Table IV, except that the isolation requirements are rescinded. The final estimate of $\not\!\!E_T$ which takes into account the electron and photon candidates described above, $\not\!\!E_T(j\mu e\gamma)$, is obtained from $\not\!\!E_T(j\mu)$ by subtracting for each electron or photon its transverse energy vector, $\vec{E}_T^{e,\gamma}$, and adding the transverse energy vector of the jet energy cluster corresponding to it, $\vec{E}_T^{j_{e,\gamma}}(cor)$:

$$\begin{aligned}\vec{\not\!\!E}_T \;&\equiv\; \vec{\not\!\!E}_T(j\mu e\gamma) \\ &=\; \vec{\not\!\!E}_T(j\mu) - \sum_{e,\gamma}\left(\vec{E}_T^{e,\gamma} - \vec{E}_T^{j_{e,\gamma}}(cor)\right).\end{aligned} \tag{6}$$

E. Photon-Lepton Samples

The selection of 29 photon-muon events and 48 photon-electron events results in the "inclusive photon-lepton sample" of 77 events total. The purpose of this paper is to sort and analyze the inclusive and exclusive combinations of particles produced for events in this sample, the method for which is summarized in Figure 3.

The first step in understanding the sample composition is through the angular separation between the lepton and the photon. A two-particle final state is indicated by the identification of a single lepton and a single photon that are nearly opposite in azimuth. Since a two-particle photon-lepton final state would violate the conservation of lepton number, such

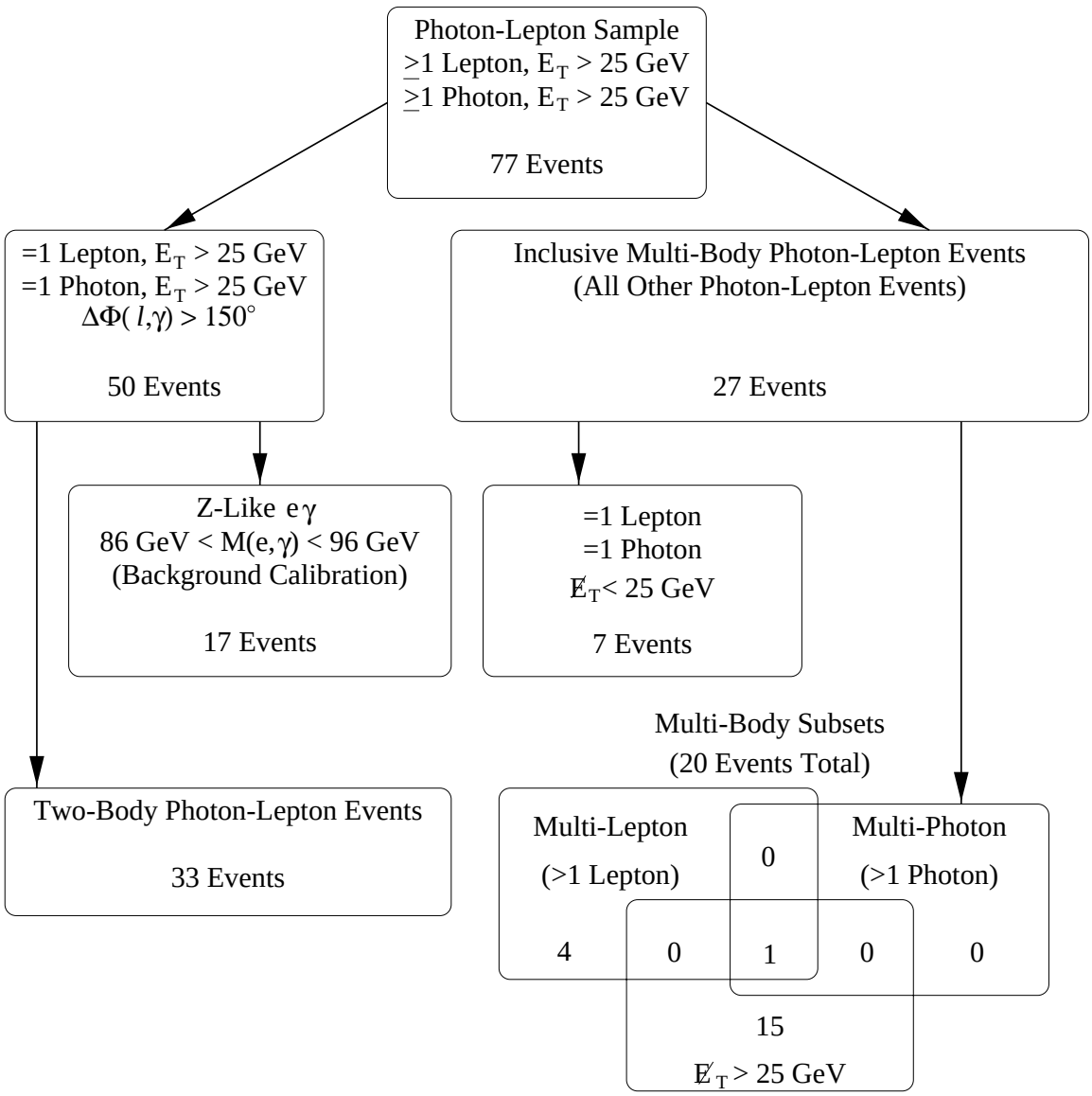

FIG. 3: The subsets of inclusive photon-lepton events analyzed in this paper. The multi-body photon-lepton subcategories of $\ell\gamma\not{E}_T$, multi-lepton, and multi-photon events are not mutually exclusive.

events arise from the standard model in one of two ways: either the lepton or photon has been misidentified, or is associated with a jet of hadrons; or a second lepton which restores conservation of lepton number has evaded identification. The former is characterized by a photon and a lepton opposite in azimuth, while the latter is suppressed in this geometry, so such a sample isolates the majority of events with misidentified photons or leptons. To

this end, the inclusive photon-lepton sample is analyzed as two subsamples: a "two-body photon-lepton sample" typical of a two-particle final state; and a "multi-body photon-lepton sample" typical of three or more particles in the final state. The selection requirements of the two-body photon-lepton sample are as follows: exactly one photon and exactly one lepton satisfying the criteria summarized in Tables I and III; no additional leptons satisfying the criteria in Table IV; and the nearest distance in azimuth between the photon and lepton, $\Delta\varphi_{\ell\gamma}$, must exceed 150°. The region $\Delta\varphi_{\ell\gamma} > 150°$ was chosen by requiring it to include 95% of Z^0 boson events decaying to two CEM electrons, which are a source of misidentified photons. Excluded from the two-body photon-lepton sample are those two-body photon-electron events for which the photon-electron invariant mass, $M_{e\gamma}$, is within 5 GeV/c^2 of M_Z. This "Z^0-like" control sample is used to estimate the photon misidentification rate from electrons, as described in Section IV C. The multi-body sample is composed of the remaining inclusive photon-lepton events.

The multi-body sample is then further analyzed for the presence of large $\not\!\!E_T$, additional leptons, or additional photons. Multi-body events with $\not\!\!E_T > 25$ GeV, the "multi-body $\ell\gamma\not\!\!E_T$ sample", and multi-body events with one or more additional photons or leptons satisfying the criteria described in Section III D, the "multi-photon and multi-lepton sample", are studied concurrently with the two-body sample and the inclusive multi-body sample. The $\not\!\!E_T$ threshold of 25 GeV was chosen from previous analyses [3, 16] as a significant indicator of a neutrino arising from leptonic decays of the W boson. Among these samples, the following properties are analyzed: the total event rate; the distribution of lepton E_T, photon E_T, and $\not\!\!E_T$; the distribution of the invariant mass of any relevant combinations of particles; and the angular distributions of any relevant combinations of particles.

IV. STANDARD MODEL SOURCES

A. $W\gamma$ and $Z^0\gamma$ Production

The dominant source of photon-lepton events at the Tevatron is electroweak diboson production, wherein an electroweak boson (W or Z^0) decays leptonically ($\ell\nu$ or $\ell\ell$) and a photon is radiated from either the initial state quark, a charged electroweak boson (W), or a charged final state lepton. The number of photon-lepton events from electroweak diboson production is estimated from a Monte Carlo event generator program [18]. The event generator program outputs 4-vectors of particles emanating from a diboson production event, and this output is used as input to a CDF detector simulation program, which outputs simulated data in a format identical to that of an actual CDF event. Simulated photon-lepton events can then be analyzed in a manner identical to that of CDF data.

The event generator program consists of a set of leading-order matrix element calculations [19] which was incorporated into the general-purpose event generator program PYTHIA [20]. The matrix element calculation for $W\gamma$ ($Z^0\gamma$) includes all tree-level diagrams with a $q\bar{q}'$ ($q\bar{q}$) initial state and a $\ell\nu_\ell\gamma$ ($\ell\ell\gamma$) final state, where ℓ is an e, μ, or τ, and the mediating electroweak boson is a real or virtual W (Z^0 or γ^*). Figure 4 shows the leading-order Feynman diagrams for $q\bar{q}' \to \ell\nu_\ell\gamma$. Figure 5 shows the leading-order Feynman diagrams for $q\bar{q} \to \ell\bar{\ell}\gamma$.

The region of phase space where the final state lepton and photon are collinear is carefully sampled, taking into account the lepton mass for each lepton flavor. This allows reliable calculations to be made for all photon-lepton separation angles and for photon E_T well below (< 1 GeV) those considered in this analysis. PYTHIA generates, fragments, and hadronizes the partons described by the matrix elements. Event rates in $p\bar{p}$ collisions are obtained

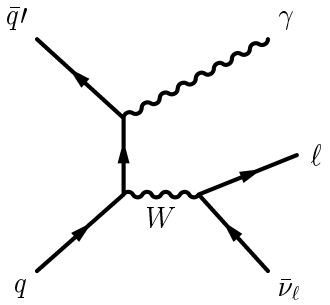

a) Initial state photon radiation

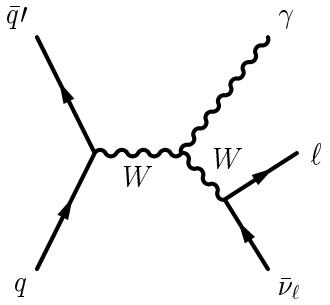

b) W final state photon radiation

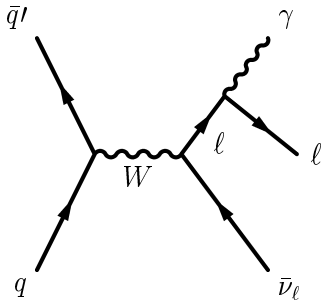

c) Lepton final state photon radiation

FIG. 4: The leading-order Feynman diagrams for photon radiation in the process $q\bar{q}\prime \to \ell\bar{\nu}_\ell\gamma$.

from the parton-level matrix elements through convolution with the leading-order proton structure function CTEQ5L [21]. The TAUOLA [22] program is used to compute the decays of any τ leptons generated. Each generated event is assigned a weight proportional to the probability of its occurrence as determined by the event rate calculation.

Generated events are used as input to a program which simulates the CDF detector response to the final state particles. The simulation includes the following features relevant to this analysis: the z_{event} distribution of $p\bar{p}$ collisions observed in CDF data, the geomet-

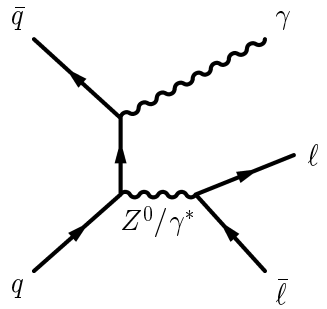

a) Initial state photon radiation

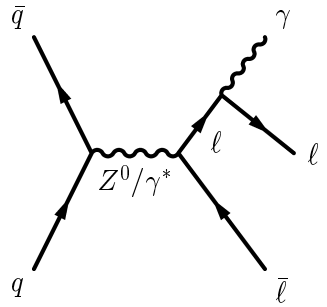

b) Lepton final state photon radiation

FIG. 5: The leading-order Feynman diagrams for photon radiation in the process $q\bar{q} \to \ell\bar{\ell}\gamma$.

ric acceptance of all CDF detector subsystems, charged tracks measured by the CTC, the tower-by-tower response of the calorimeters to final state particles, the CES response to electromagnetic showers, and the response of the central muon chambers to penetrating charged particles. The program is not used to simulate the CDF trigger, the z_{event} distribution beyond $|z_{event}| = 60$ cm, nor the energy-out-of-time distribution; the event selection efficiencies for these must be applied as separate corrections to the simulated event rates. There also exist 6-8% differences between the lepton (and photon) detection efficiencies found in CDF data and the efficiencies similarly computed in simulated data, as described in Section III. Simulated event rates containing particles of type X are therefore adjusted by a ratio C_X of detection efficiencies in CDF data to that of simulated events,

$$C_X \;=\; \epsilon^{data}_{XID}/\epsilon^{sim}_{XID}, \tag{7}$$

where ϵ_{XID}^{data} is the detection efficiency of X in CDF data and ϵ_{XID}^{sim} is the corresponding efficiency in simulated data. The detection efficiencies are obtained from samples of Z boson candidates decaying to pairs of leptons, specifically those events which have one lepton candidate satisfying the selection criteria of Tables III and IV, a second lepton candidate satisfying the fiducial and kinematic selection criteria from those Tables, and a dilepton mass $M_{\ell\ell}$ within 10 GeV/c^2 of M_Z. The efficiency is extracted from that fraction of events where the second lepton satisfies all selection criteria. Photon identification efficiency is similarly measured with electron pair data. Particle identification efficiencies in simulated data are obtained with the same procedure using a sample of Z boson events created by the PYTHIA event generator and a detector simulation. The systematic uncertainty of C_X is estimated to be half of the difference between C_X and unity. Table V lists the corrections for the various types of leptons and photons analyzed.

Simulated events with PEM electrons are an exception to this procedure, since the PEM shower shape quantity $\chi^2_{3\times3}$ is not included in the detector simulation. The PEM electron detection efficiency for all the requirements in Table IV, except the $\chi^2_{3\times3}$ requirement, is measured and corrected for in the same way as other leptons; the correction is listed in Table V. The efficiency of the $\chi^2_{3\times3}$ requirement for PEM electrons which satisfy all other requirements, $\epsilon_{PEM\ \chi^2}$, is then measured separately using CDF data to be $95.0 \pm 0.5\%$ [14]. This is an additional correction to the identification efficiency for simulated events with PEM electrons.

The complete set of correction factors to the detection efficiencies of simulated events, C_{sim}, is given by

$$C_{sim} \;=\; \epsilon_{z60} \times \epsilon_{EOT} \times \prod_X C_{XID}^{N_X} \times \epsilon_{PEM\ \chi^2}^{N_{PEM}}, \tag{8}$$

where

Particle	ϵ_{XID}^{data}	ϵ_{XID}^{sim}	C_{XID}
CEM photon	0.86	0.93	0.93 ± 0.04
CEM electron	0.81	0.88	0.92 ± 0.04
2nd CEM electron	0.89	0.97	0.91 ± 0.05
PEM electron	0.92	0.99	0.94 ± 0.03
FEM electron	0.75	0.98	0.77 ± 0.12
central muon	0.93	0.99	0.94 ± 0.03
CMI muon	0.91	0.99	0.92 ± 0.04

TABLE V: Corrections to the simulated particle identification efficiencies obtained from CDF data [14]. Included are the efficiencies measured directly from CDF data (ϵ_{XID}^{data}), the efficiencies measured from simulated data (ϵ_{XID}^{sim}), and the corrections to simulated rates (C_{XID}).

- ϵ_{z60} is the efficiency for the requirement $|z_{event}| < 60$ cm, measured to be 0.95 ± 0.02.
- ϵ_{EOT} is the efficiency for the requirement $E_T(\text{out-of-time}) = 0$, measured to be 0.975 ± 0.004 [3].
- $\prod_X C_{XID}^{N_X}$ is the product, over each type X of lepton or photon identified in this analysis, of corrections C_{XID} to the simulated particle identification efficiencies listed in Table V. Each factor has an exponent N_X equal to the number of particles of type X identified by the detector simulation.
- and $\epsilon_{PEM\ \chi^2}^{N_{PEM}}$ is an additional correction factor for PEM electrons, measured to be 0.953 ± 0.005 and described above, with an exponent N_{PEM} equal to the number of PEM electrons identified by the detector simulation.

The mean contribution to photon-lepton candidates in CDF data, $\bar{N}_{\ell\gamma}$, for a particular generated process is given by

$$\bar{N}_{\ell\gamma} = \sigma_{LO} \times K_{NLO} \times \epsilon_{trig} \times C_{sim} \times \int Ldt \times (\sum w_{pass})/(\sum w_{tot}), \quad (9)$$

Item	Value	Relative Uncertainty
K_{NLO}	1.30 ± 0.10	7.7%
σ_{LO}	105.0 ± 5.3 pb	5.0%
$\sum w_{pass} / \sum w_{tot}$	$(2.57 \pm 0.12) \times 10^{-4}$	4.7%
ϵ_{trig}	0.985 ± 0.015	1.5%
C_{sim}	0.792 ± 0.052	6.6%
$\int Ldt$	86.34 ± 3.52 pb^{-1}	4.1%
$\bar{N}_{e\gamma}$	2.36 ± 0.31	13.1%

TABLE VI: The mean number of multi-body photon-electron events, $\bar{N}_{e\gamma}$, expected from $W(\rightarrow e\nu) + \gamma$. The factors used in Equation 9 and their uncertainties are also shown.

where

- σ_{LO} is the leading order cross section computed by the event generator for a given process with a given set of generator-level selection requirements and thresholds. The uncertainty due to generator statistics is negligible. The uncertainty due to PDF normalization is taken to be $\pm 5\%$, as recommended in [23].

- K_{NLO} is the next-to-leading order (NLO) QCD K-factor for $W\gamma$ ($Z^0\gamma$) production estimated from NLO calculations [24]. The K-factors used are 1.30 ± 0.10 for $W\gamma$ production and 1.25 ± 0.05 for $Z^0\gamma$ production, where the uncertainties are estimated from the QCD renormalization scale dependence of the NLO cross section.

- ϵ_{trig} is the trigger efficiency for photon-lepton events. For photon-electron events $\epsilon_{trig} = 98.5 \pm 1.5\%$; for photon-muon events ϵ_{trig} varies with muon type and photon E_T, with an average efficiency of 94% for simulated $W\gamma$ events satisfying all selection criteria. The uncertainty of the photon-muon trigger efficiency is $\pm 6\%$ [14].

- C_{sim} is the product of the correction factors to the detection efficiencies computed by the CDF detector simulation, as described above.

- $\int Ldt$ is the integrated luminosity for the 1994-5 run employed in this analysis, 86.34 ± 3.52 pb^{-1} [25].

- $\sum w_{pass}$ is the sum of the weights of the simulated events satisfying all selection criteria. The uncertainty is given by $\sqrt{\sum w_{pass}^2}$, which is typically a few percent.

- $\sum w_{tot}$ is the sum of the weights of all simulated events, with uncertainty given by $\sqrt{\sum w_{tot}^2}$, which is typically negligible.

Table VI shows a sample calculation for multi-body photon-electron events originating from $W(\rightarrow e\nu) + \gamma$ production. The uncertainty in the mean rate has roughly equal contributions from the NLO K-factor, simulation systematics, luminosity, proton structure, and generator statistics. Other simulated processes have similar uncertainties.

	Two-Body Events		Multi-Body Events		Multi-Body Events	
Process	$e\gamma X$	$\mu\gamma X$	$e\gamma X$	$\mu\gamma X$	$e\gamma \not\!\!E_T X$	$\mu\gamma \not\!\!E_T X$
$\gamma + W$ production						
$\gamma + W \rightarrow \ell\nu$	1.1 ± 0.1	1.4 ± 0.2	2.4 ± 0.3	2.5 ± 0.3	1.9 ± 0.3	1.9 ± 0.3
$\gamma + W \rightarrow \tau\nu$	0.08 ± 0.02	0.09 ± 0.02	0.08 ± 0.02	0.06 ± 0.01	0.04 ± 0.01	0.05 ± 0.01
Subtotal	1.2 ± 0.2	1.5 ± 0.2	2.4 ± 0.3	2.5 ± 0.3	1.9 ± 0.3	2.0 ± 0.3
$\gamma + Z^0$ production						
$\gamma + Z^0 \rightarrow \ell\ell$	5.1 ± 0.5	6.5 ± 0.8	4.9 ± 0.5	4.5 ± 0.5	0.3 ± 0.1	0.9 ± 0.1
$\gamma + Z^0 \rightarrow \tau\tau$	0.3 ± 0.1	0.5 ± 0.1	0.13 ± 0.03	0.10 ± 0.02	0.03 ± 0.01	0.05 ± 0.01
Subtotal	5.4 ± 0.6	7.1 ± 0.8	5.0 ± 0.5	4.6 ± 0.5	0.3 ± 0.1	1.0 ± 0.2
Total	6.6 ± 0.7	8.6 ± 1.0	7.5 ± 0.8	7.1 ± 0.8	2.3 ± 0.3	3.0 ± 0.4

TABLE VII: The estimated $W\gamma$ and $Z^0\gamma$ backgrounds for two-body photon-lepton events, inclusive multi-body photon-lepton events, and multi-body $\ell\gamma \not\!\!E_T$ events. There exist correlated uncertainties between the different photon-lepton sources. The symbol X denotes the allowed inclusion of any other combination of particles, except where explicitly prohibited.

Table VII shows the results of all simulated processes, for inclusive two-body events, inclusive multi-body events, and multi-body $\ell\gamma \not\!\!E_T$ events. The slightly larger contribution

of two-body $\mu\gamma$ events relative to $e\gamma$ events is due to the explicit exclusion of $e\gamma$ events whose invariant mass is "Z^0-like" (86 GeV/c^2 $< M_{e\gamma} <$ 96 GeV/c^2). There are no significant differences between the inclusive multi-body rates for $e\gamma$ and $\mu\gamma$ production. In the case of $Z^0\gamma$ production, there is a larger number of multi-body $\mu\gamma\not\!\!E_T$ events (1.0) relative to $e\gamma\not\!\!E_T$ events (0.3). The difference is due to events where the second muon falls outside the solid angle in which muons can be detected ($|\eta_\mu| > 1.2$), subsequently inducing missing E_T equal to the p_T of the second muon. Leptons from τ decays contribute to the total photon-lepton rate at a level far below the leptonic branching ratio of a τ (about 3% accepted compared to a leptonic branching ratio of 18%) because the average lepton E_T is much lower than that of leptons from the direct decay of a W or Z^0.

Table VIII shows the results of all simulated processes for multi-body photon-lepton events with additional leptons or photons, respectively. More $ee\gamma$ events than $\mu\mu\gamma$ events are expected due to the larger detector acceptance for additional electrons, which are identified in the central, plug, and forward calorimeters.

B. Jets Misidentified as Photons

A jet of hadrons initiated by a final state quark or gluon can contain mesons which decay to photons, such as the π^0, η, or ω. If one or more of these photons constitute a sufficiently large fraction of the jet momentum, then the hadron jet can be misidentified by the CDF detector as a single prompt photon. Such a jet, when produced in association with a lepton candidate, contributes to the detected photon-lepton candidates.

The contribution of lepton plus misidentified jet events is determined by counting the number of jets in CDF lepton data, $N_{\ell jet}$, and then multiplying that number by an estimate of the probability of a jet being misidentified as a photon, P_γ^{jet}, to obtain the number of

	Multi-Body Events				
Process	$ee\gamma$	$\mu\mu\gamma$	$e\mu\gamma$	$e\gamma\gamma$	$\mu\gamma\gamma$
$\gamma + W$ production					
$\gamma + W \to \ell\nu$	—	—	—	—	—
$\gamma + W \to \tau\nu$	—	—	—	—	—
Subtotal	—	—	—	—	—
$\gamma + Z^0$ production					
$\gamma + Z^0 \to \ell\ell$	3.3 ± 0.4	2.2 ± 0.3	—	0.012 ± 0.012	0.004 ± 0.004
$\gamma + Z^0 \to \tau\tau$	—	—	0.05 ± 0.01	—	—
Subtotal	3.3 ± 0.4	2.2 ± 0.3	0.05 ± 0.01	0.012 ± 0.012	0.004 ± 0.004
Total	3.3 ± 0.4	2.2 ± 0.3	0.05 ± 0.01	0.012 ± 0.012	0.004 ± 0.004

TABLE VIII: The estimated $W\gamma$ and $Z^0\gamma$ backgrounds for multi-body photon-lepton samples with additional leptons and photons.

photon-lepton candidates,

$$N_{\ell\gamma} = N_{\ell jet} \times P_{\gamma}^{jet}. \tag{10}$$

Lepton-jet candidates are selected from inclusive electron and muon triggers as follows. The Level 1 trigger and Level 3 trigger requirements are identical to those enumerated in Sections III B and III C of Section 3. The Level 2 trigger requirements differ from those of the photon-lepton sample due to the absence of the photon. Electron-jet events must be accepted by a Level 2 electron trigger, which requires a CEM energy cluster with $E_T > 16$ GeV; the ratio E_{HAD}/E_{EM} for that cluster < 0.125; and a CFT track matching the CEM cluster with $p_T > 12$ GeV/c. The efficiency of these electron trigger requirements has been measured to be $\epsilon_e = 90.9 \pm 0.3\%$ [16]. Muon-jet events are selected from the Level 2 inclusive muon triggers, which have the same efficiency as the muon triggers described in Section III B, except that they are prescaled due to bandwidth limitations. The prescaling results in a

reduction of the trigger efficiency by a factor of 0.43 ± 0.02 for CMX muons, 0.43 ± 0.02 for CMNP muons, and 1.0 (no prescale) for CMUP muons. Requiring a Level 2 muon trigger precludes the use of CMP or CMU muons.

The requirements for lepton-jet candidates are as follows: one or more lepton candidates satisfying the criteria in Table III; and one or more jets with $|\eta_j| < 1.0$, jet $E_T > 25$ GeV, and a separation distance of the jet from the lepton in $\eta - \varphi$ space, $\Delta R_{\ell j}$, greater than 0.5. As a further step to prevent electrons from Z^0 boson decays being counted as jets, jet candidates must have electron-jet separation $\Delta R_{ej} > 0.5$ for all central electrons satisfying the selection criteria for additional electrons listed in Table IV. Table X shows the raw total number of jets, summed over all lepton-jet candidate events, for the various signal regions of this analysis.

Because the lepton trigger requirements of the lepton-jet sample are less efficient than the trigger requirements of the photon-lepton sample, the effective number of jets which potentially contribute to the photon-lepton candidates must be augmented by a ratio of the efficiencies of the different trigger paths. For electron-jet events with exactly one electron, this is simply a constant, $\epsilon_{e\gamma}/\epsilon_e = 1.08 \pm 0.02$; for muon-jet events with exactly one muon, the efficiency ratio, $R_{\mu_i\gamma}$, varies with muon stub type and jet E_T,

$$R_{\mu_i\gamma} = \frac{\epsilon_{\mu_i} + (1 - \epsilon_{\mu_i}) \times \epsilon_\gamma(E_T)}{P_{\mu_i}\epsilon_{\mu_i}} \tag{11}$$

where ϵ_{μ_i} is the trigger efficiency for muons of stub type i, P_{μ_i} is the inclusive muon trigger prescale factor for muons of stub type i, and $\epsilon_\gamma(E_T)$ is the trigger efficiency of the photon candidate a jet would produce in the event of jet misidentification, as a function of photon E_T. This ratio is evaluated for each jet in each event, and the sum over all jets in all events gives the total effective number of jets. Because CMU and CMP muons have been excluded from the lepton-jet sample, the number of jets in muon-jet events must be additionally

multiplied by a factor of 1.14 ± 0.03 to compensate for the acceptance lost relative to that of photon-lepton events. This lost acceptance was calculated from the $W\gamma$ and $Z\gamma$ simulation described in Section IV A.

For lepton-jet events with multiple leptons, the presence of the additional lepton increases the efficiency of the lepton trigger requirements, and the efficiency ratio of such events relative to the corresponding photon-lepton events must be accounted for separately. For electron-jet events with an additional CEM electron, the trigger efficiency for both electron-jet and photon-electron events is nearly 100%, so that the trigger efficiency ratio of such events is assumed to be unity. Electron-jet events with additional PEM or FEM electrons have the same efficiency ratio as that of single electron-jet events above. For muon-jet events with an additional CMNP, CMUP, or CMX muon, the trigger efficiency ratio depends upon the muon trigger efficiencies of the two muon stub types:

$$R_{\mu_i\mu_j\gamma} \;=\; \frac{\epsilon_{\mu_i\mu_j} + (1 - \epsilon_{\mu_i\mu_j}) \times \epsilon_\gamma(E_T)}{P_{\mu_i}\epsilon_{\mu_i} + (1 - P_{\mu_i}\epsilon_{\mu_i}) \times P_{\mu_j}\epsilon_{\mu_j}}, \tag{12}$$

where ϵ_{μ_i} and ϵ_{μ_j} are the muon trigger efficiencies of the two different muon stub types, P_{μ_i} and P_{μ_j} are the inclusive muon trigger prescales of the two different muon stub types, and $\epsilon_{\mu_i\mu_j}$ is the efficiency of the logical OR of the two muon triggers,

$$\epsilon_{\mu_i\mu_j} \;\equiv\; \epsilon_{\mu_i} + (1 - \epsilon_{\mu_i}) \times \epsilon_{\mu_j}. \tag{13}$$

Muon-jet events with additional CMU, CMP, or CMI muons have the same efficiency ratio as that of single muon-jet events above.

The total effective number of jets in lepton-jet candidate events after all corrections have been applied is also given in Table X. There are more electron-jet candidates than muon-jet candidates because the angular coverage of the CEM is larger than that of the central muon chambers, particularly at higher lepton $|\eta|$. Comparing Table X with Tables VII and VIII,

it is concluded that in order to measure photon-lepton processes with electroweak-sized cross sections and a signal-to-background ratio greater than 1:1, P_{γ}^{jet} must be less than approximately 10^{-3}.

Mesons which decay to photons are typically only a portion of a shower of hadrons initiated by a high E_T quark or gluon. Other hadrons in the shower will deposit energy in the calorimeter close to the electromagnetic shower produced by these photons. Prompt photons (or electrons, which shower similarly) produced in the hard scattering of partons do not exhibit additional nearby energy in the calorimeters; the additional E_T measured in a cone of $R = 0.4$ around the electromagnetic shower position, E_{cone}^{iso}, therefore serves as a discriminant between prompt photons and misidentified jets. This discriminant is already employed in the photon selection (Table I), by requiring $E_{cone}^{iso} < 2$ GeV. If the distribution of E_{cone}^{iso} is relatively flat for misidentified jets, the distribution of E_{cone}^{iso} of the photon candidates which fail this requirement can be extrapolated linearly to estimate the number of misidentified jets which satisfy it.

The probability that a jet is misidentified as a photon is determined from samples of jets and photons in events with a lepton trigger. Lepton candidates in lepton-triggered jet events are selected with the same trigger requirements as the lepton-jet sample described above. Instead of applying the full lepton selection criteria in Table III, the minimal set of Level 3 lepton trigger requirements, listed in Table II, is applied in this selection, so as to maximize the sample size. Along with exactly one such loose lepton candidate, lepton-triggered jet events are required to have exactly one jet with $|\eta_j| < 1.0$, $E_T > 25$ GeV, and $\Delta R_{\ell j} > 0.5$. The lepton-triggered jet sample consists of 46091 electron-triggered jet events and 12875 muon-triggered jet events.

Lepton candidates in lepton-triggered photon events are selected with the same trigger

requirements as the lepton-triggered jet events described above, except that the prescaled Level 2 inclusive muon trigger requirements are replaced by the muon-jet trigger described in Section III B. Lepton-triggered photon events are required to have exactly one loose lepton candidate as above, and are required to have exactly one photon candidate satisfying all of the photon selection criteria in Table I, except for the isolation requirements. Specifically, the requirement that the sum of the p_T of all tracks in a cone of $R = 0.4$ around the photon be less than 5 GeV/c is rescinded, and the E_{cone}^{iso} requirement is loosened from 2 GeV to 12 GeV. The lepton-triggered photon sample consists of 121 photon-electron and 38 photon-muon events.

Since the muon-triggered jet sample has a less efficient trigger path than the muon-triggered photon sample, an unbiased comparison of the two samples requires that the number of muon-triggered jet events must be augmented on an event-by-event basis by the ratio of trigger efficiencies of the two samples. The ratio for each event in this case is simply the inverse of the Level 2 muon trigger prescale factor for the stub type of the muon, $1/P_{\mu_i}$. The effective number of muon-triggered jet events increases from 12875 to 17745.

Photon candidates in the lepton-triggered photon sample consist of a combination of prompt photons, electrons misidentified as photons, and jets misidentified as photons, where only the jet component is relevant to the evaluation of P_γ^{jet}. The distribution of E_{cone}^{iso} of the other two components is measured using a sample of CEM electrons from Z^0 decays. Dielectron events are selected from events satisfying the same trigger criteria as that of the photon-electron candidates described in Section III C. From these triggers, Z^0-like dielectron events are selected which have exactly two CEM electrons passing the electron criteria in Table III, excepting the isolation requirement (that the total E_T deposited in the calorimeters, in a cone of $R = 0.4$ around the electron track, be less than 10% of the electron E_T),

and which have dielectron invariant mass within 5 GeV of M_Z. The distribution of E_{cone}^{iso} normalized to unity, dN_Z/dE_{cone}^{iso}, for the 3300 electrons in this sample is shown in Figure 6. CEM electron showers—which have the same calorimeter response as CEM showers from prompt photons—exhibit $E_{cone}^{iso} < 2$ GeV 95% of the time.

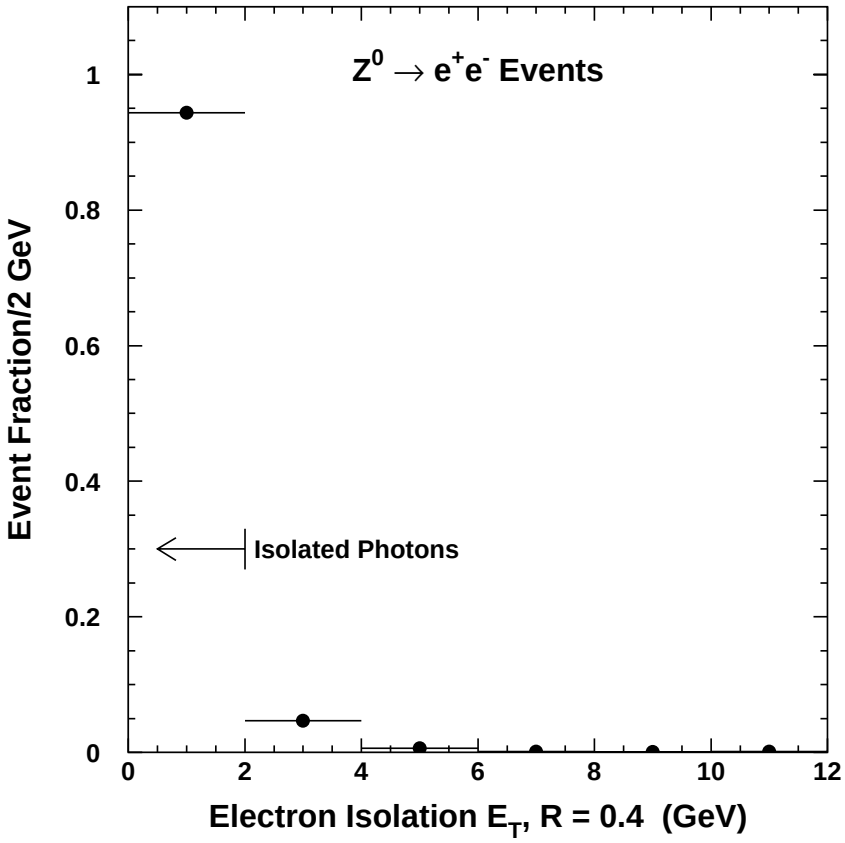

FIG. 6: The distribution of E_{cone}^{iso} for CEM electrons from Z^0 decays, normalized to unity.

Using the measured distribution dN_Z/dE_{cone}^{iso} for prompt photons or electrons, and assuming a linear distribution in E_{cone}^{iso} for jets misidentified as photons, the total number of photon candidates as a function of E_{cone}^{iso}, dN/dE_{cone}^{iso}, is given by

$$\frac{dN}{dE_{cone}^{iso}} = A_1 \times \frac{dN_Z}{dE_{cone}^{iso}} + A_2 + A_3 \times E_{cone}^{iso}, \tag{14}$$

where A_1, A_2, and A_3 are free parameters to be fit to the data. If the bin size is chosen to be equal to the E_{cone}^{iso} threshold for isolated photon candidates (2 GeV), then the number of prompt photon (or electron misidentified as photon) candidates with $E_{cone}^{iso} < 2$ GeV is given by

$$A_1 \times \left.\frac{dN_Z}{dE_{cone}^{iso}}\right|_{bin\ 1} = A_1 \times 0.95, \tag{15}$$

and the number of jets misidentified as photons with $E_{cone}^{iso} < 2$ GeV is given by

$$\left. A_2 + A_3 \times E_{cone}^{iso}\right|_{bin\ 1} = A_2 + A_3 \times 1 \text{ GeV}. \tag{16}$$

If in addition the normalization of the distribution is chosen to be the ratio of the number of lepton-triggered photon events (121 photon-electron and 38 photon-muon) to that of the effective number of lepton-triggered jet events (46091 electron-jet and 17745 muon-jet), then $A_2 + A_3 \times 1$ GeV is identically the jet misidentification rate P_γ^{jet}.

Employing these conventions, the distribution dN/dE_{cone}^{iso} for lepton-triggered photon events is shown in Figure 7. The distribution (solid points) is peaked in the first bin corresponding to isolated photon candidates, followed by a linearly falling tail of non-isolated photon candidates. The minimum χ^2 fit of the data to the functional form of Equation 14 (solid line) is shown in Figure 7, along with the linear portion of the fit obtained from A_2 and A_3 (dashed line). The functional form chosen describes the data well (χ^2/d.o.f. $= 0.38$), yielding an average jet misidentification rate P_γ^{jet} of $3.8 \pm 0.7 \times 10^{-4}$. The best fit parameters are shown in Table IX.

Also shown in Figure 7 is an estimate of dN/dE_{cone}^{iso} obtained from a simulation of W-jet production (cross-hatched histogram), using the PYTHIA event generator and the detector simulation described in Section IV A. The leading-order Feynman diagrams for W-jet production employed by the PYTHIA event generator are shown in Figure 8. Simulated events

are selected which satisfy the same requirements as the lepton-triggered jet and lepton-triggered photon samples obtained from the data, and photon candidates are required to arise solely from hadron decay. The simulated results for dN/dE_{cone}^{iso} exhibit a shape consistent with a linear functional form, as well as a magnitude consistent with the observed jet misidentification rate.

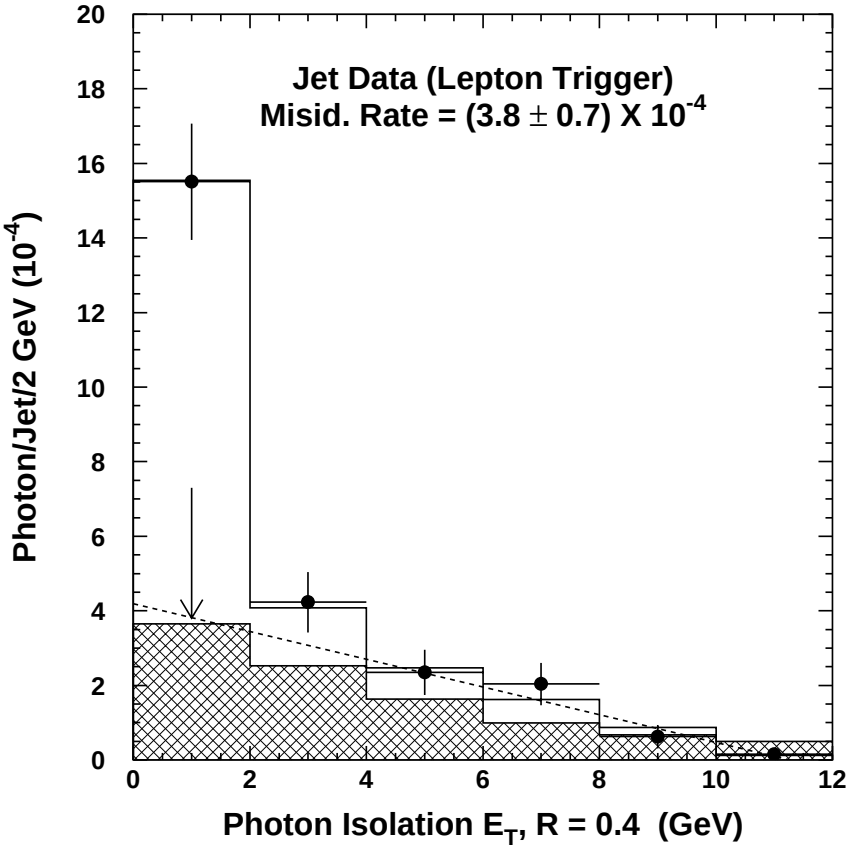

FIG. 7: The number of photon candidates per jet, as a function of E_{cone}^{iso}, for CDF jet data obtained with a lepton trigger. Included are the results of CDF data (points), the fit of CDF data to Equation 14 (solid line), the linear portion of the same fit (dotted line), an estimate of this distribution from a simulation of W plus jet events performed by PYTHIA (cross-hatched histogram), and an arrow indicating the value of P_{γ}^{jet}.

Figure 9 shows the distribution dN/dE_{cone}^{iso} computed for electron-triggered photon events and muon-triggered photon events separately. The separate jet misidentification rates ob-

	Lepton-Jet Samples		
	ej	μj	ℓj
Photons	121	38	159
Jets	46091	17745	63836
$A_1(10^{-4})$	13 ± 2	14 ± 4	13 ± 2
$A_2(10^{-4})$	4.7 ± 0.9	2.4 ± 1.5	4.2 ± 0.7
$A_3(10^{-4}/\text{GeV})$	-0.4 ± 0.1	-0.2 ± 0.2	-0.4 ± 0.1
$P_\gamma^{jet}(10^{-4})$	4.3 ± 1.0	2.2 ± 1.5	3.8 ± 0.7
χ^2/d.o.f.	0.38	0.44	0.42

TABLE IX: The results of fitting dN/dE_{cone}^{iso} to photon candidates in CDF jet data obtained with a lepton trigger. Included are the number of photons and jets in each sample, the best fit parameters A_i, the χ^2 per degree of freedom for the fit, and the jet misidentification rate P_γ^{jet}.

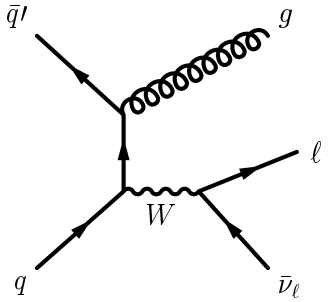

a) $q\bar{q}' \to Wg$

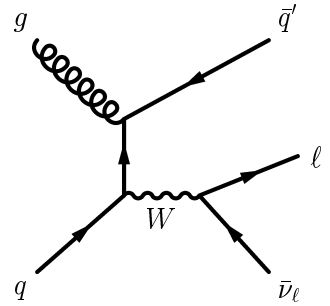

b) $qg \to W\bar{q}'$

FIG. 8: The leading-order Feynman diagrams for W-jet production.

tained from these distributions, also shown in Table IX, are statistically consistent with each other.

Additional evidence for the linear behavior of dN/dE_{cone}^{iso} in misidentified jets is obtained

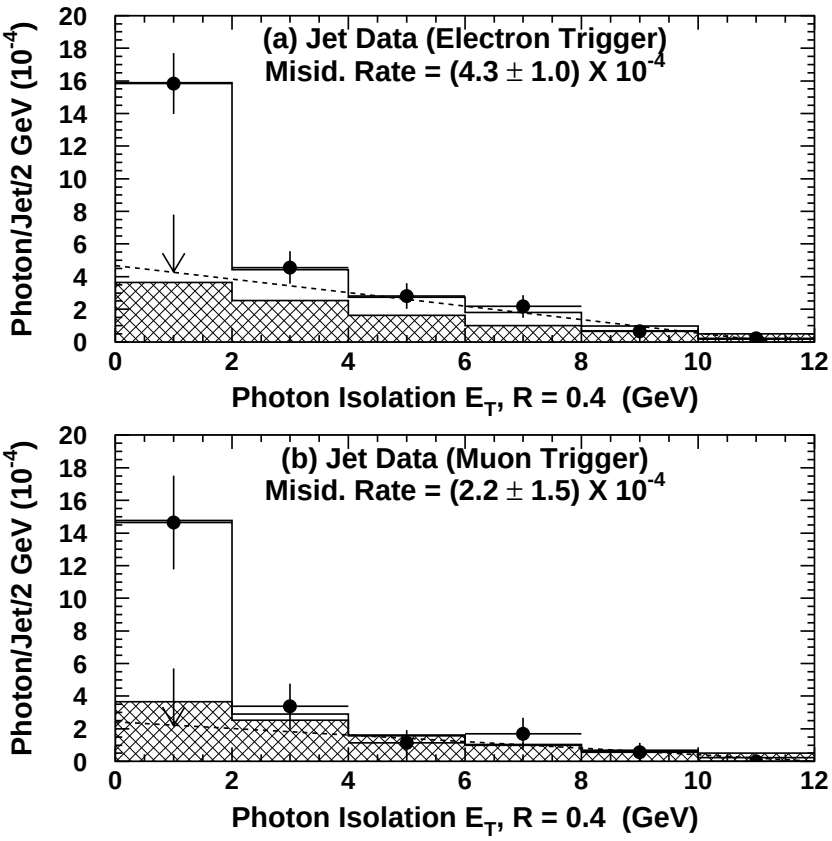

FIG. 9: The number of photon candidates per jet, as a function of E_{cone}^{iso}, for CDF jet data obtained with (a) an electron trigger or (b) a muon trigger. Included are the results of CDF data (points), the fit of CDF data to Equation 14 (solid line), the linear portion of the same fit (dotted line), an estimate of this distribution from a simulation of W plus jet events performed by PYTHIA (cross-hatched histogram), and an arrow indicating the value of P_{γ}^{jet}.

from a sample of lepton-triggered events enriched with π^0's. Lepton candidates in these lepton-triggered π^0 events are selected with the same trigger requirements as the lepton-triggered photon events described above. Lepton-triggered π^0 events are required to have exactly one loose lepton candidate as above, and are required to have exactly one π^0 candidate which satisfies requirements similar to photon candidates in Table I, with the following differences: the isolation requirements are not applied, as done for the lepton-triggered photon sample; the requirements for additional CES energy clusters are not applied; and

the χ^2_{avg} is required to be *greater* than 20. The lepton-triggered π^0 sample consists of 38 electron-π^0 and 11 muon-π^0 events.

The distribution dN/dE^{iso}_{cone} for lepton-triggered π^0 events is shown in Figure 10. The distribution (solid points) is consistent with that of a linearly decreasing tail. Also shown in Figure 10 is an estimate of dN/dE^{iso}_{cone} obtained from a simulation of W-jet production (cross-hatched histogram) as described above, except with the lepton-triggered π^0 selection applied. As with lepton-triggered photons, the simulated results for dN/dE^{iso}_{cone} exhibit a shape consistent with a linear functional form, as well as a magnitude consistent with the observed π^0 rate.

Table X shows the mean number of photon-lepton events expected to originate from misidentified jets, for the various subsets of photon-lepton events to be analyzed. The uncertainties in these estimates are dominated by the uncertainty in P^{jet}_{γ}, which in turn is limited in precision by the number of exclusive photon-lepton events. The total number of two-body and multi-body events expected is 1-2 events per category per lepton species, with roughly equal contributions in photon-electron and photon-muon events. The number of multi-lepton events arising from misidentified jets is an order of magnitude smaller. The number of $e\mu\gamma$, $e\gamma\gamma$, and $\mu\gamma\gamma$ events arising from misidentified jets is negligible, due to the small number of jets in $e\mu$, $e\gamma$, and $\mu\gamma$ events, respectively.

C. Electrons Misidentified as Photons

The dominant source of misidentifed particles in photon-electron events is $Z^0 \rightarrow e^+e^-$ production, wherein one of the electrons undergoes hard photon bremsstrahlung in the detector material, or the CTC fails to detect one of the electron tracks, and that electron is subsequently misidentified as a prompt photon. There are approximately 1000 central

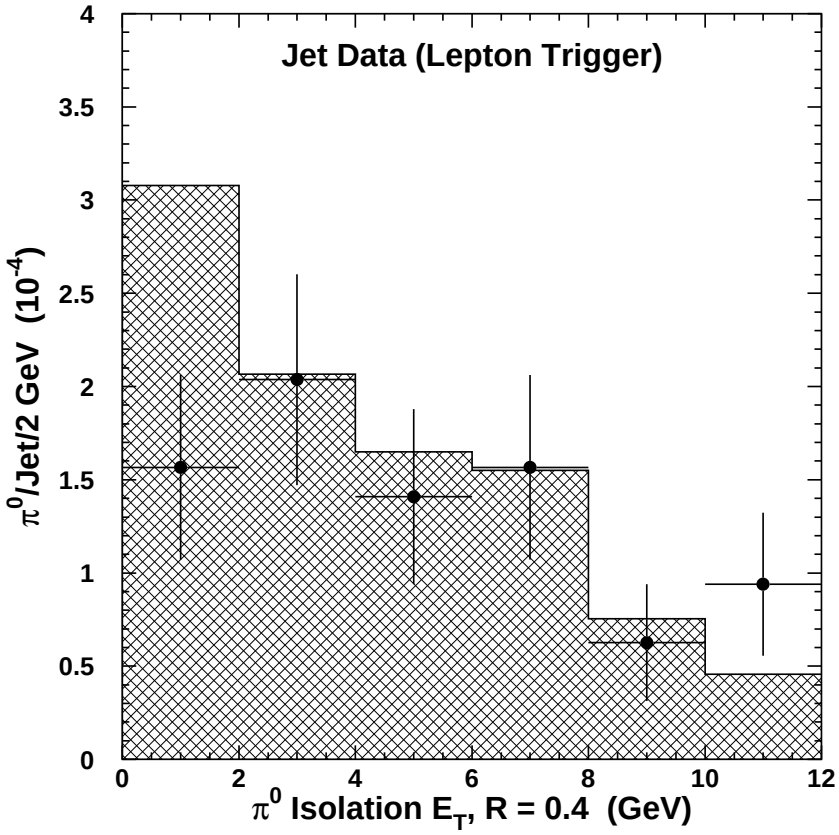

FIG. 10: The number of π^0 candidates per jet, as a function of E_{cone}^{iso}, for CDF jet data obtained with a lepton trigger. Included are the results of CDF data (points) and an estimate of this distribution from a simulation of W plus jet events performed by PYTHIA (cross-hatched histogram).

electron pairs in the CDF data, so a electron misidentification rate as low as 1% will give rise to 20 photon-electron events, which would be unacceptably high for finding sources of new physics comparable to $W/Z^0 + \gamma$ production (see Tables VII and VIII). It is therefore necessary to either obtain independently the electron misidentification rate to sufficient accuracy that a background subtraction can be performed, or to assume that those photon-electron events in the CDF data which are sufficiently similar in their kinematics to Z^0 production are not a significant source of new physics, and that such events may be used to estimate misidentified photon-electron events elsewhere. The latter method is employed in

	N_{raw}	$N_{\ell jet}$	$N_{\ell\gamma}$
Two-Body Events			
$e\gamma X$	4530	4909	1.9 ± 0.3
$\mu\gamma X$	1983	3844	1.5 ± 0.3
Multi-Body Events			
$e\gamma X$	4235	4565	1.7 ± 0.3
$\mu\gamma X$	2024	3855	1.5 ± 0.3
$e\gamma \not\!\!E_T X$	2584	2798	1.1 ± 0.2
$\mu\gamma \not\!\!E_T X$	1369	2633	1.0 ± 0.2
$ee\gamma X$	479	496	0.19 ± 0.03
$\mu\mu\gamma X$	226	346	0.13 ± 0.02
$e\mu\gamma X$	16	19	—
$e\gamma\gamma X$	3	3	—
$\mu\gamma\gamma X$	3	4	—

TABLE X: The contributions $N_{\ell\gamma}$ to the various categories of photon-lepton candidates from jets misidentified as photons, using the measured jet misidentification rate $3.8 \pm 0.7 \times 10^{-4}$. Included are the raw number N_{raw} of jets in inclusive lepton data and the effective number of jets $N_{\ell jet}$ which potentially contribute to each category.

what follows.

A control sample of Z^0-like events is selected from photon-electron candidates with the following requirements: exactly one photon and exactly one electron satisfying the criteria summarized in Tables I and III; no additional leptons satisfying the criteria in Table IV; the nearest distance in azimuth between the photon and the electron, $\Delta\varphi_{e\gamma}$, must exceed 150°; and the invariant mass of the photon-electron pair, $M_{e\gamma}$, must be within 5 GeV/c^2 of the Z^0 mass (91 GeV/c^2). There are 17 such events in the CDF data, and their characteristics are shown in Figure 11. In order to check the assumption that these are predominantly $Z^0 \to e^+e^-$ events, a sample of $Z^0 \to e^+e^-$ events is selected from the inclusive electron sample which have exactly two electrons passing the electron criteria in Table III, and which have the same kinematic requirements as the photon-electron control sample. There are 1235

such events, and their distributions, normalized to the photon-electron control sample, are also shown in Figure 11; the shapes of the distributions of the two samples are statistically consistent with each other.

Some of the photon-electron events in the control sample will arise from real photons from $W/Z^0 + \gamma$ production, or from jets misidentified as photons. In order to avoid double-counting these as a source of background, the diboson Monte Carlo calculations described in Section IV A and the jet misidentification calculations described in Section IV B are used to estimate the number of photon-electron events passing the control sample requirements, and this is subtracted from the total number of control sample events to give a corrected of misidentified photon-electron events. Out of 17 events, 1.24 ± 0.13 events (1.01 ± 0.12 from diboson events, 0.23 ± 0.04 from misidentified jets) on average are expected to have real photons, which are subtracted to give 15.8 ± 4.3 misidentified photon-electron events in the control sample.

The number of misidentified photon-electron events in the control sample, $N_{e\gamma}^{ctrl}$, divided by the number of electron-electron events with the same kinematics, N_{ee}^{ctrl}, gives the misidentified photon-electron rate per central electron pair. For any other particular subset of central electron pairs, the total contribution to the corresponding photon-electron sample is the product of the number of central electron pairs with this misidentification rate. For multi-body photon-lepton events, a sample of dielectron events is selected from events satisfying the same trigger criteria as that of the photon-electron candidates described in Section III C. From these triggers a sample of multi-body dielectron events is selected which has exactly two electrons satisfying the electron criteria in Table III, and which has the same angular separation requirements ($\Delta\varphi_{ee} < 150°$) as the multi-body photon-lepton sample. There are 132 such events. The estimated number of misidentified photon-electron

events in multi-body photon-electron events is therefore

$$N_{e\gamma}^{mult} = [(15.8 \pm 4.3)/1235] \times 132$$
$$= 1.7 \pm 0.5 \text{ events.} \quad (17)$$

Similar calculations are made for the other photon-lepton samples analyzed, and the results are summarized in Table XI. The number of multi-photon and multi-lepton events is negligible, due to the low number of $ee\gamma$ and eee events in the CDF data.

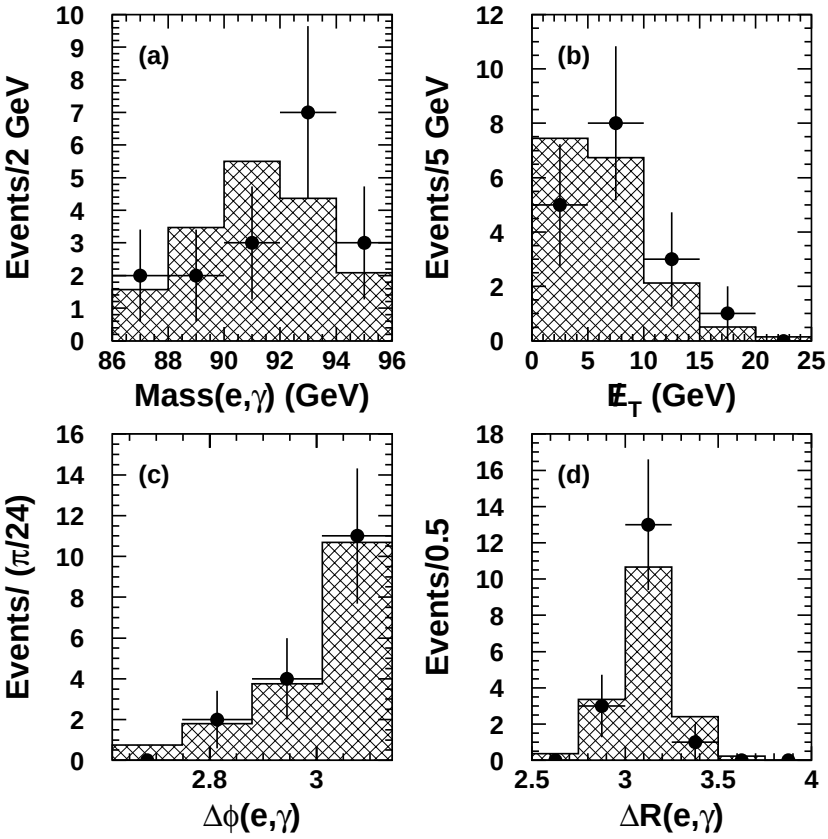

FIG. 11: The distributions for (a) $M_{e\gamma}$, (b) $\not\!\!E_T$, (c) $\Delta\varphi_{e\gamma}$, and (d) $\Delta R_{e\gamma}$ in Z^0-like events. The points are the Z^0-like photon-electron sample; the cross-hatched histogram is electron-electron events from CDF data with the same kinematic requirements, normalized to the control sample.

	N_{ee}	$N_{e\gamma}$
Two-Body $e\gamma X$	321	4.1 ± 1.1
Multi-Body $e\gamma X$	132	1.7 ± 0.5
Multi-Body $e\gamma \not\!\!E_T X$	8	0.10 ± 0.04

TABLE XI: The expected mean number of photon-electron candidates $N_{e\gamma}$ from Z^0 electrons misidentified as photons, for the various categories analyzed. The number of dielectron events N_{ee} which potentially contribute to each category is also included.

D. Light Hadrons Misidentified as Muons

A hadron jet can contain charged hadrons, which may occasionally penetrate the calorimeters and be detected by the muon chambers, ("hadron punchthrough"), or which may decay to a muon before reaching the calorimeters ("hadron decay-in-flight"). If one of these hadrons constitutes a sufficiently large fraction of the jet momentum, then the hadron jet can be misidentified by the CDF detector as a single prompt muon. Such a jet produced in association with a photon candidate contributes to the detected photon-muon candidates. The contribution of photon plus misidentified jet events is determined by analyzing a sample of isolated, high-momentum tracks in CDF photon data, determining the probability of each track being misidentified as a muon, and computing the total contribution by summing this probability over all tracks in the sample.

Starting with the inclusive photon events described in Section III A, a photon-track sample is selected by requiring one or more photon candidates satisfying the criteria in Table I and one or more CTC tracks with $p_T > 25$ GeV/c which extrapolate to the CMU, CMP, or CMX detectors. The selected CTC tracks must also satisfy the same track requirements as those of muon tracks, as described in Section III B: a minimum of six layers of CTC wire measurements, at least three of which must be axial wire measurements and at least 2 of

which must be stereo wire measurements; an impact parameter $d_0 < 0.3$ cm; the distance in z of the CTC track to the primary event vertex $|\Delta z_{event}| < 5$ cm; and, as an isolation requirement, the sum of the momenta of other CTC tracks incident upon a cone of $R = 0.4$ around the candidate track direction must be less than 10% of the p_T of the candidate track. The photon-track sample consists of 394 events containing 398 track candidates.

Because the photon trigger requirements of the photon-track sample are less efficient than the trigger requirements of the photon-muon sample, the effective number of tracks which potentially contribute to the photon-muon candidates must be augmented by a ratio of the efficiencies of the different trigger paths, for each track in each event of the sample. The efficiency ratio $R_{\gamma t}$ varies with photon E_T and the muon stub type μ_i that the track t would produce in the event of hadron punchthrough or decay-in-flight:

$$R_{\gamma t} = \frac{\epsilon_{\mu_i} + (1 - \epsilon_{\mu_i}) \times \epsilon_\gamma(E_T)}{\epsilon_\gamma(E_T)}, \tag{18}$$

where ϵ_{μ_i} is the trigger efficiency for muons of stub type i, and $\epsilon_\gamma(E_T)$ is the trigger efficiency of photon candidates as a function of photon E_T.

The fraction of track candidates which give rise to hadron punchthrough is computed from the number of hadronic interaction lengths traversed through the calorimeter to a muon chamber, for high-momentum pions and kaons. The thickness of the CDF calorimeter, typically 5 absorption lengths for pions and 4.4 lengthx for kaons, corresponds to a hadron rejection factor of about 150 (80) for the CMU (CMX). The CMP is additionally shielded from hadrons by 60 cm of steel, which effectively absorbs all incident hadrons; the contribution of hadron punchthrough to CMP or CMUP muon candidates is henceforth assumed to be negligible. The contribution to hadron punchthrough of hadrons which partially shower in the calorimeter is reduced to a negligible level by the muon identification requirements of low calorimeter activity and a small track-stub matching distance. It is

therefore sufficient to consider only the case where a hadron traverses the entire length of the calorimeter without interacting, and subsequently enters the CMU or CMX.

For each track in the photon-track sample, the probability of the track becoming hadron punchthrough, $P^t_{PT_\mu}$, is given by

$$\begin{aligned} P^t_{PT_\mu} &= F_\pi \times \exp\left(-\lambda_\pi(E^t)/\sin\theta_t\right) \\ &\quad + F_K \times \exp\left(-\lambda_K(E^t)/\sin\theta_t\right), \end{aligned} \tag{19}$$

where F_π and F_K are the relative $\pi : K$ fractions; and $\lambda_\pi(E^t)$ and $\lambda_K(E^t)$ are the calorimeter thicknesses in units of the interaction lengths [26] for the corresponding particle type, as a function of the total energy E^t of the track t and the sign of its charge. The interaction length for kaons is longer than that of pions, so P_{PT_μ} is a maximum for $F_K = 1.0$ and a minimum for $F_K = 0.0$. For the central value estimate, an experimentally measured value $F_K = 0.33$ is used [27], with upper and lower systematic bounds defined by $F_K = 1.0$ and $F_K = 0.0$. This systematic uncertainty is the dominant uncertainty for the hadron punchthrough estimates.

Stub Type	Two-Body	Multi-Body	Multi-Body
	$\mu\gamma X$	$\mu\gamma X$	$\mu\gamma \not\!\!E_T X$
CMUP	—	—	—
CMNP	0.37	0.12	0.07
CMX	0.15	0.08	0.03
CMP	—	—	—
CMU	0.90	0.25	0.09
Total	1.42 ± 0.74	0.45 ± 0.25	0.18 ± 0.11

TABLE XII: The contribution to the photon-muon candidates of punchthrough hadrons misidentified as muons, indexed by muon stub type, for various categories analyzed.

For any particular subset of the photon-track sample, the total contribution to the corresponding photon-muon sample is the sum over all candidate tracks of the hadron

punchthrough probabilities, weighted by the appropriate trigger efficiency ratio for each track:

$$N_{PT\mu} = \sum_t R_{\gamma t} \times P^t_{PT\mu}. \tag{20}$$

For example, in the case of multi-body $\mu\gamma$ events, a subset of the punchthrough candidates is selected for which the track extrapolates to the CMU or CMX detectors, and $\Delta\varphi$ between the photon and the track is less than 150°. There are 89 such tracks, corresponding to a background of 0.45 ± 0.25 events from hadron punchthrough in the inclusive multi-body $\mu\gamma$ sample. Of these 89 tracks, 32 belong to events with $\not\!\!E_T > 25$ GeV, corresponding to 0.18 ± 0.11 punchthrough events in the multi-body $\mu\gamma\not\!\!E_T$ sample. The results indexed by muon stub type are shown in Table XII.

Each of the photon-track events described above also potentially contributes to photon-muon events in the form of hadron decay-in-flight; hadrons which decay to muons prior to interacting with the central calorimeters will satisfy the requirements of prompt muons. The inner radius of the central calorimeters is 1.73 m, and the radius beyond this corresponding to one hadronic interaction length is approximately 2 m; hadrons decaying prior to a radius of 2 m are therefore likely to be misidentified as muons.

For each track in the photon-track sample, the hadron decay-in-flight probability $P^t_{DIF\mu}$ is given by

$$\begin{aligned} P^t_{DIF\mu} = {} & F_\pi \times \mathrm{B}R(\pi^\pm \to \mu\nu) \\ & \times(1 - \exp(-(2.0/c\tau_\pi)(m_\pi/cp_T))) \\ & + F_K \times \mathrm{B}R(K^\pm \to \mu\nu) \\ & \times(1 - \exp(-(2.0/c\tau_K)(m_K/cp_T))), \end{aligned} \tag{21}$$

where p_T is the transverse momentum of the track t, in GeV/c; F_π is the fraction of tracks

which are pions, BR($\pi^{\pm} \to \mu\nu$) is the branching ratio of pions to muons (~ 1.0), $c\tau_{\pi}$ is the pion proper decay length in meters (7.8 m), and m_{π} is the pion mass (0.140 GeV); F_K is the fraction of tracks which are kaons, BR($K^{\pm} \to \mu\nu$) is the branching ratio of kaons to muons (0.635), $c\tau_K$ is the kaon proper decay length in meters (3.7 m), and m_K is the kaon mass (0.494 GeV). For tracks with transverse momentum of 25 GeV/c, the decay-in-flight probability is 0.67% for kaons and 0.14% for pions.

For any particular subset of the photon-track sample, the contribution to the corresponding photon-muon candidates of decay-in-flight hadrons is the sum over all tracks of the decay-in-flight probabilities, augmented by the trigger efficiency ratio:

$$N_{DIF\mu} = \sum_t R_{\gamma t} \times P^t_{DIF\mu} \tag{22}$$

Due to the shorter kaon lifetime, the upper and lower bounds are again determined by the results assuming kaon fractions of 1.0 and 0.0, respectively, with the central value determined by $F_K = 0.33$. The results indexed by muon stub type are shown in Table XIII. The contributions relative to those sources of photon-muon events considered previously are small.

Stub Type	Two-Body	Multi-Body	Multi-Body
	$\mu\gamma X$	$\mu\gamma X$	$\mu\gamma \not\!\!E_T X$
CMUP	0.35	0.10	0.03
CMNP	0.15	0.04	0.02
CMX	0.21	0.11	0.03
CMP	0.08	0.04	0.01
CMU	—	—	—
Total	0.80 ± 0.89	0.28 ± 0.31	0.10 ± 0.11

TABLE XIII: The contribution to the photon-muon candidates of decay-in-flight hadrons misidentified as muons, indexed by muon stub type, for the various categories analyzed.

E. Heavy-Flavored Hadron Decay to Leptons

A hadron consisting of one or more quarks with heavy flavor (charm or bottom) has a much shorter lifetime than those hadrons considered in Section IV D; at the Tevatron, heavy-flavored hadrons typically travel a few millimeters before decaying and do not produce a measurable track in the CTC. Consequently, the decay in flight of heavy-flavored hadrons to leptons is not accounted for in the estimates of Section IV D, which infer the number of decay-in-flight hadrons from CTC tracks. The contribution to photon-lepton candidates that arises from heavy-flavored hadrons produced in association with a prompt photon is instead accounted for through Monte Carlo event generation and detector simulation, as in Section IV A.

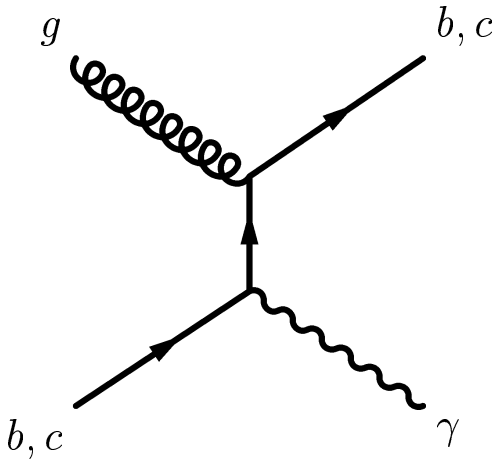

FIG. 12: The leading-order Feynman diagram for $\gamma + b, c$ production.

Figure 12 shows the leading-order Feynman diagram for a heavy-flavored quark produced in association with a prompt photon. The leading-order matrix element for this process is calculated with the PYTHIA [20] event generator program, using the leading-order proton structure function CTEQ5L [21]. PYTHIA also generates, fragments, and hadronizes the partons produced in a simulated interaction. The QQ program, based on measurements of

the CLEO experiment [28], is used to compute the decays of heavy-flavored hadrons. Previous measurements of photon-heavy-flavor events at the Tevatron [29] indicate agreement of CDF data with next-to-leading order QCD predictions. In order to obtain agreement of the leading order simulation with next-to-leading order cross section predictions, a next-to-leading order K-factor is applied to the leading order cross section computed by PYTHIA. In the previous measurements this K-factor was found to be $K_{NLO} = 1.9 \pm 0.2$. Using this K-factor and the leading-order cross section computed by PYTHIA ($\sigma_{LO} = 7$ nb), the mean contribution to photon-lepton candidates in CDF data for this process is given by Equation 9 in Section IV A.

Table XIV shows, for the various signal regions of this analysis, the number of simulated events which are photon-lepton candidates, N_{MC}, out of 117 million events (equivalent to 8.4 fb^{-1}) generated; and the mean contribution expected in 86.34 pb^{-1} of CDF data, $N_{\ell\gamma}$. The contributions expected are small compared to those discussed in Sections IV A–IV D. All simulated candidates are found to be two-body photon-lepton events, as would be expected for a process with a two-body final state. Contributions to multi-body photon-lepton events are bounded from above by 0.01 at the 68% confidence level, and are henceforth assumed to be negligible.

V. ANALYSIS OF PHOTON-LEPTON CANDIDATES

The objectives of this analysis are the comparison of the observed event totals, in the various photon-lepton samples described in Section III E, with the totals predicted by the standard model, and the similar comparison of the distributions of kinematic properties in those samples. New physics in small samples of events would most likely manifest itself as an excess of observed events over expected events. In the absence of a specific alternative

	N_{MC} (8.4 fb^{-1})	$N_{\ell\gamma}$
Two-Body Events		
$e\gamma X$	10	0.07 ± 0.02
$\mu\gamma X$	3	0.03 ± 0.01
Multi-Body Events		
$e\gamma X$	0	< 0.01
$\mu\gamma X$	0	< 0.01
$e\gamma \not\!\!E_T X$	0	< 0.01
$\mu\gamma \not\!\!E_T X$	0	< 0.01

TABLE XIV: The contribution to photon-lepton candidates, $N_{\ell\gamma}$, of heavy-flavored hadrons decaying to leptons, for the various categories analyzed. Included is the number of candidate events N_{MC} produced by the simulation for each category.

model, the significance of an observed excess is computed from the likelihood of obtaining the observed number of events, assuming that the null hypothesis (i.e., the standard model) is correct. This "observation likelihood", denoted here by $P(N \geq N_0|\mu_{SM})$, is defined as that fraction of the Poisson distribution of expected events (with a mean μ_{SM} predicted by the standard model) which yields outcomes N greater than or equal to that observed in CDF data, N_0. A small observation likelihood is indicative of a sample which is potentially better explained by physics beyond the standard model.

For each photon-lepton sample, the mean event total predicted by the standard model, μ_{SM}, is the sum of each of the sources discussed in Section IV. The uncertainty in μ_{SM} is the standard deviation of a large ensemble of calculations. For each calculation in the ensemble, each quantity used to compute photon-lepton event sources (simulation systematics, integrated luminosity, photon and lepton misidentification rates, etc.) varies randomly as a Gaussian distribution, where the center of the distribution is the mean value of the quantity and the width is the uncertainty of the quantity. This ensemble of calculations accounts for correlated uncertainties between the various contributing sources, such as the uncertainty in

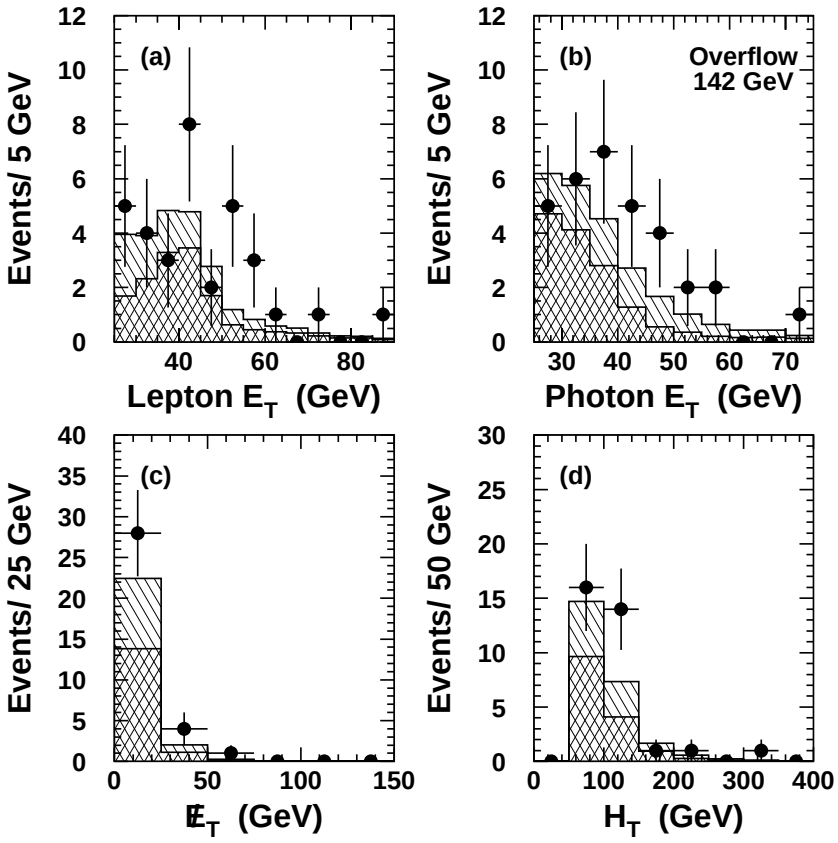

FIG. 13: The distributions for (a) lepton E_T, (b) photon E_T, (c) $\not\!\!E_T$, and (d) H_T in two-body photon-lepton events. The points are CDF data, the hatched histogram is the total predicted mean background, and the cross-hatched histogram is the predicted mean diboson background.

the integrated luminosity used to normalize the various simulated event totals. The observation likelihood $P(N \geq N_0|\mu_{SM})$ is again computed from a large ensemble of calculations. For each calculation in the ensemble, each quantity used to compute photon-lepton event sources again varies randomly as a Gaussian distribution, and the resulting mean event total is used to randomly generate a Poisson distributed outcome N. The fraction of calculations in the ensemble with outcomes $N \geq N_0$ gives $P(N \geq N_0|\mu_{SM})$.

The total standard model predictions for the distributions of kinematic properties are the sums of the distributions of the corresponding properties of each of the sources discussed

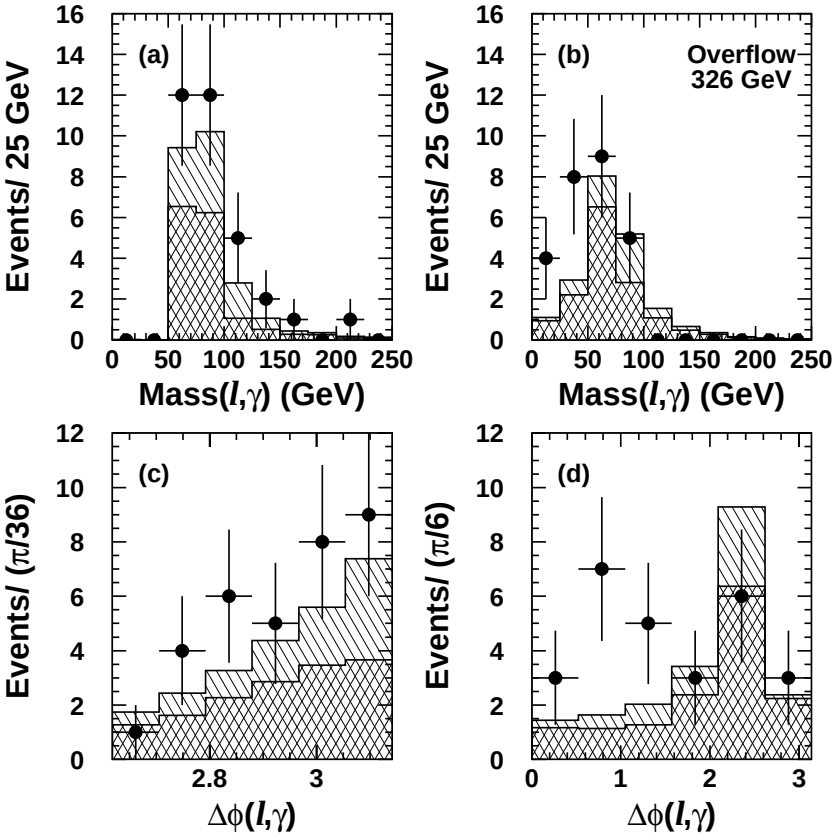

FIG. 14: The distributions for (a) $M_{\ell\gamma}$ in two-body photon-lepton events, (b) $M_{\ell\gamma}$ in inclusive multi-body photon-lepton events, (c) $\Delta\varphi_{\ell\gamma}$ in two-body photon-lepton events, and (d) $\Delta\varphi_{\ell\gamma}$ in inclusive multi-body photon-lepton events. The points are CDF data, the hatched histogram is the total predicted mean background, and the cross-hatched histogram is the predicted mean diboson background.

in Section IV. For the contribution from jets misidentified as photons, the appropriately weighted distributions of jet properties in lepton-jet events are used in the predicted distributions of photon properties. Similarly, for the contribution from electrons misidentified as photons the distributions of electron properties in electron-electron events are used to predict distributions of photon properties, and for the contribution from hadrons misidentified as muons the distributions of track properties in photon-track events are used to predict distributions of muon properties.

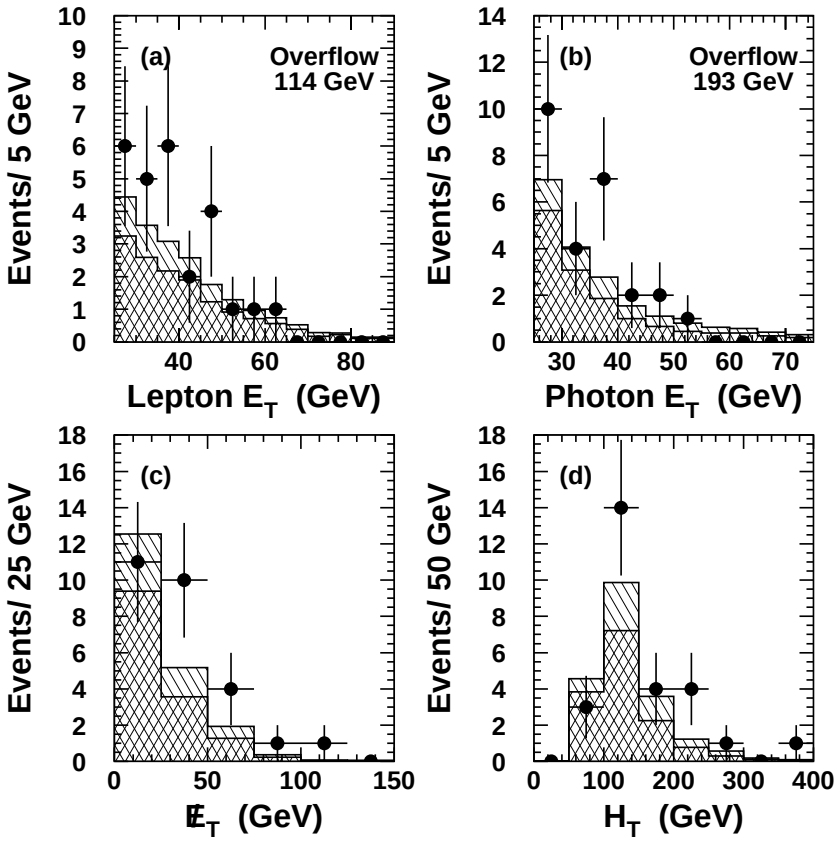

FIG. 15: The distributions for (a) lepton E_T, (b) photon E_T, (c) $\not\!\!E_T$, and (d) H_T in inclusive multi-body photon-lepton events. The points are CDF data, the hatched histogram is the total predicted mean background, and the cross-hatched histogram is the predicted mean diboson background.

A. Two-Body and Inclusive Multi-Body Photon-Lepton Events

The predicted and observed totals for two-body photon-lepton events are compared in Table XV. The mean predicted contributions from each of the sources discussed in Section IV are also listed. Half of the predicted total originates from $Z^0\gamma$ production where one of the charged leptons has evaded identification; the other half originates from roughly equal contributions of $W\gamma$ production, misidentified jets, misidentified electrons, and misidentified charged hadrons. The observed photon-electron total is somewhat higher than predicted, with an observation likelihood of 4.3%; the observed photon-muon total is in excellent agree-

Process	$e\gamma X$	$\mu\gamma X$	$\ell\gamma X$
W+γ	1.2 ± 0.2	1.5 ± 0.2	2.7 ± 0.3
Z+γ	5.4 ± 0.6	7.1 ± 0.8	12.5 ± 1.2
ℓ+jet, jet $\rightarrow \gamma$	1.9 ± 0.3	1.5 ± 0.3	3.3 ± 0.7
$Z \rightarrow ee, e \rightarrow \gamma$	4.1 ± 1.1	—	4.1 ± 1.1
Hadron+γ	—	1.4 ± 0.7	1.4 ± 0.7
π/K Decay+γ	—	0.8 ± 0.9	0.8 ± 0.9
b/c Decay+γ	0.07 ± 0.02	0.03 ± 0.01	0.10 ± 0.03
Predicted μ_{SM}	12.6 ± 1.4	12.3 ± 1.8	24.9 ± 2.4
Observed N_0	20	13	33
$P(N \geq N_0 \mid \mu_{SM})$	0.043	0.46	0.093

TABLE XV: The mean number μ_{SM} of two-body photon-lepton events predicted by the standard model, the number N_0 observed in CDF data, and the observation likelihood $P(N \geq N_0|\mu_{SM})$. There exist correlated uncertainties between the different photon-lepton sources.

ment with the predicted total, however, so that the observation likelihood of the two-body photon-lepton event total increases to 9.3%.

The predicted and observed distributions of the kinematic properties of two-body photon-lepton events are compared in Figures 13 and 14. Superimposed upon the distributions of the total contribution predicted by the standard model are the distributions of the contribution from standard model diboson production.

Figure 13 shows the distributions of photon E_T, lepton E_T, and $\not\!\!E_T$ for the events. The observed distributions of photon and lepton E_T exhibit the range of values expected from the standard model. The number of two-body photon-lepton events observed with $\not\!\!E_T < 25$ GeV is in good agreement with the predicted total. There are 5 events observed with $\not\!\!E_T > 25$ GeV, whereas 2.3 events are expected, a result which is potentially related to that observed in multi-body $\ell\gamma\not\!\!E_T$ events described below.

The distribution of the total E_T of all objects in the event, H_T, is also included in

Figure 13. It is defined as the sum of the magnitudes of $\not\!\!E_T$ and the transverse energies of all electrons, muons, photons, and jets in the event:

$$H_T \equiv \not\!\!E_T + \sum_e E_T^e + \sum_\mu cp_T^\mu + \sum_\gamma E_T^\gamma + \sum_j E_T^j(cor). \quad (23)$$

The jets included in this sum are required to have $E_T^j(raw) > 8$ GeV and $|\eta_j| < 2.4$, just as in Equation 4. Large H_T is correlated with the production of massive particles, virtual or real. The observed data exhibit the range of H_T values expected.

Process	$e\gamma X$	$\mu\gamma X$	$\ell\gamma X$
W+γ	2.4 ± 0.3	2.5 ± 0.3	5.0 ± 0.6
Z+γ	5.0 ± 0.5	4.6 ± 0.5	9.6 ± 0.9
ℓ+jet, jet $\to \gamma$	1.7 ± 0.3	1.5 ± 0.3	3.2 ± 0.6
$Z \to ee, e \to \gamma$	1.7 ± 0.5	—	1.7 ± 0.5
Hadron+γ	—	0.5 ± 0.3	0.5 ± 0.3
π/K Decay+γ	—	0.3 ± 0.3	0.3 ± 0.3
b/c Decay+γ	< 0.01	< 0.01	< 0.01
Predicted μ_{SM}	10.9 ± 1.0	9.3 ± 1.0	20.2 ± 1.7
Observed N_0	11	16	27
$P(N \geq N_0 \mid \mu_{SM})$	0.52	0.037	0.10

TABLE XVI: The mean number μ_{SM} of inclusive multi-body photon lepton events predicted by the standard model, the number N_0 observed in CDF data, and the observation likelihood $P(N \geq N_0|\mu_{SM})$. There exist correlated uncertainties between the different photon-lepton sources.

The predicted and observed totals for inclusive multi-body photon-lepton events are compared in Table XVI. The magnitude of the predicted total is similar to that of two-body photon-lepton events. About half of the predicted total originates from $Z^0\gamma$ production, a quarter from $W\gamma$ production, and the remaining quarter from particles misidentified as photons or leptons. In this sample the observed photon-muon total is higher than predicted, with an observation likelihood of 3.7%; all of the difference can be attributed to events

with large $\not\!\!E_T$, as discussed below. The observed photon-electron total is in excellent agreement with the predicted total, and the observation likelihood of the inclusive multi-body photon-lepton total increases to 10%.

The predicted and observed distributions of the kinematic properties of inclusive multi-body photon-lepton events are compared in Figures 14 and 15. The difference between the observed and predicted totals can be entirely attributed to events with $\not\!\!E_T > 25$ GeV; the observed events with lower $\not\!\!E_T$ agree with predictions. There is also a larger proportion of observed events than expected with smaller photon-lepton azimuthal separation, $\Delta\varphi_{\ell\gamma}$, for which the contributions from misidentified photons or leptons are largely absent.

B. Multi-Body $\ell\gamma\not\!\!E_T$ Events

The predicted and observed totals for multi-body $\ell\gamma\not\!\!E_T$ events are compared in Table XVII. For photon-electron events, requiring $\not\!\!E_T > 25$ GeV suppresses the contribution from $Z^0\gamma$ production and from electrons misidentified as photons, which have no intrinsic $\not\!\!E_T$, while preserving the contribution from $W\gamma$ production. As a result, 57% of the predicted $e\gamma\not\!\!E_T$ total arises from $W\gamma$ production, 31% from jets misidentified as photons, only 3% from $Z^0\gamma$ production, and the remaining 9% from other particles misidentified as photons. The observed $e\gamma\not\!\!E_T$ total agrees with the predicted total, with a 25% probability that the predicted mean total of 3.4 events yields 5 observed events. Included in the 5 events observed is the $ee\gamma\gamma\not\!\!E_T$ event.

For photon-muon events, requiring $\not\!\!E_T > 25$ GeV does not completely eliminate the contribution from $Z^0\gamma$, for if the second muon has $|\eta| > 1.2$ and $p_T > 25$ GeV/c it evades all forms of muon detection and induces the necessary amount of $\not\!\!E_T$. The rate at which this occurs is estimated well by $Z^0\gamma$ event simulation, however, since it is solely a function of

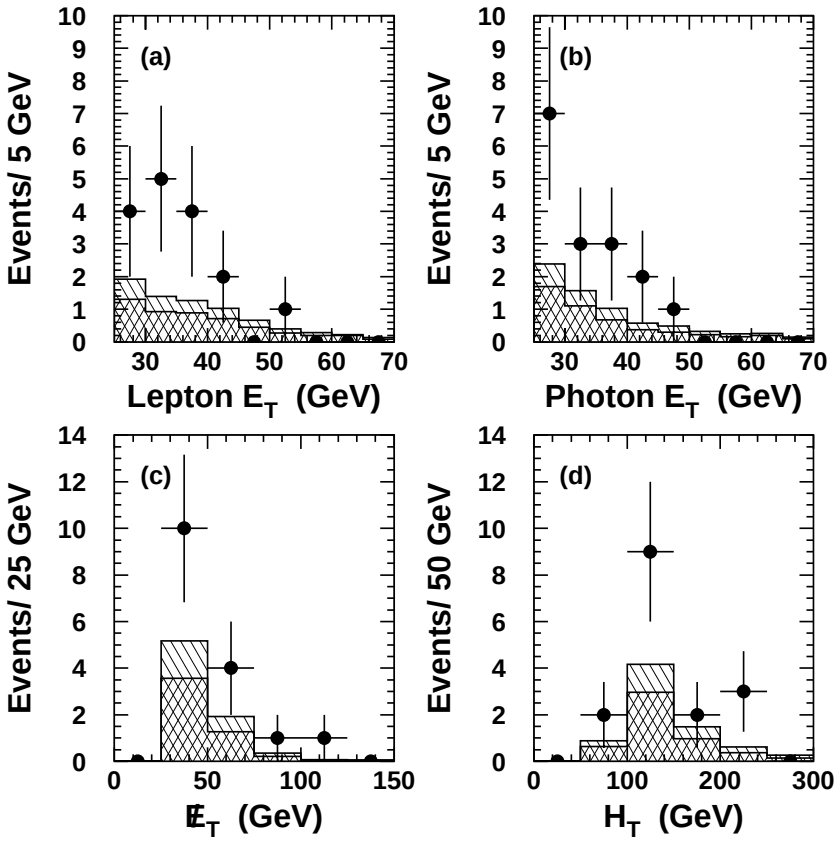

FIG. 16: The distributions for (a) lepton E_T, (b) photon E_T, (c) $\not\!\!E_T$, and (d) H_T in multi-body $\ell\gamma\not\!\!E_T$ events. The points are CDF data, the hatched histogram is the total predicted mean background, and the cross-hatched histogram is the predicted mean diboson background.

the CDF detector acceptance for such a second muon. Of the 4.6 multi-body photon-muon events predicted to originate from $Z^0\gamma$ production, 2.2 events are predicted to contain a second visible muon, 1.0 are predicted to induce more than 25 GeV of $\not\!\!E_T$ as above, and 1.4 are predicted to induce less than 25 GeV of $\not\!\!E_T$. As shown in Table XVIII, 1 event is observed with a second visible muon, in agreement with $Z^0\gamma$ predictions. The predicted total for multi-body $\mu\gamma\not\!\!E_T$ events consists of 47% $W\gamma$ production, 24% events with jets misidentified as photons, 23% $Z^0\gamma$ production, and the remaining 7% from other particles misidentified as muons.

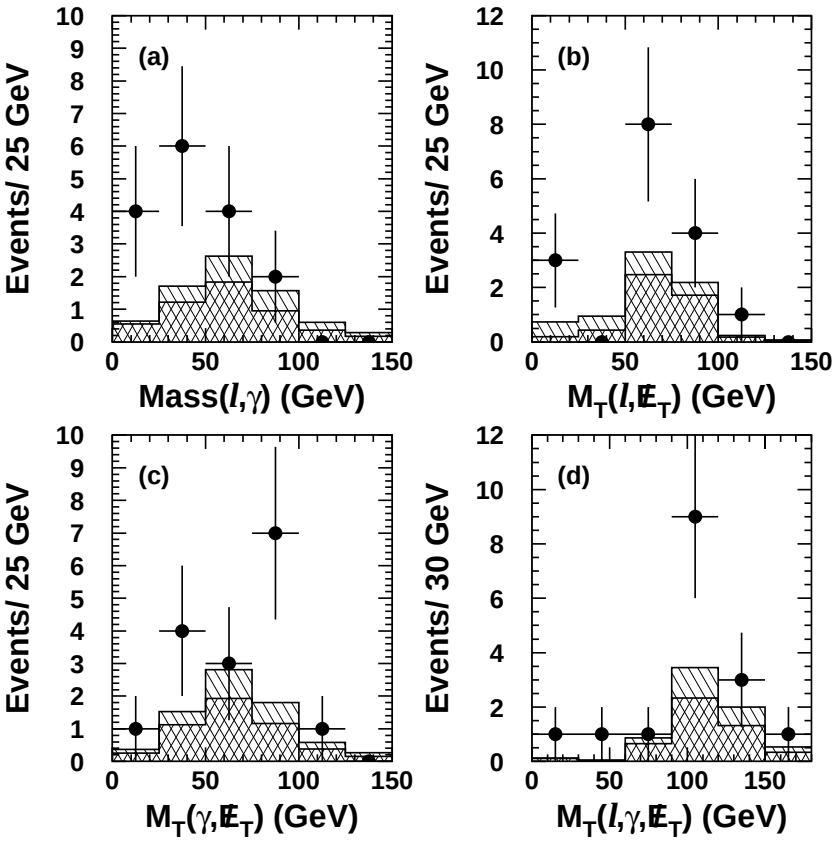

FIG. 17: The distributions for (a) photon-lepton mass, (b) lepton-$\not\!\!E_T$ transverse mass, (c) photon-$\not\!\!E_T$ transverse mass, and (d) $\ell\gamma\not\!\!E_T$ transverse mass in multi-body $\ell\gamma\not\!\!E_T$ events. The points are CDF data, the hatched histogram is the total predicted mean background, and the cross-hatched histogram is the predicted mean diboson background.

The observed $\mu\gamma\not\!\!E_T$ total is much higher than predicted (11 observed vs. 4 expected), with an observation likelihood of only 0.54%; the observation likelihood of the $\ell\gamma\not\!\!E_T$ total is only slightly higher at 0.72%.

The predicted and observed distributions of the kinematic properties of multi-body $\ell\gamma\not\!\!E_T$ events are compared in Figures 16–18. The photon E_T, lepton E_T, $\not\!\!E_T$, and H_T observed are within the range expected from the standard model. The observed photon E_T spectrum has more events near the 25 GeV threshold than expected. However, nearly all photon candidates are one standard deviation or more above threshold in terms of the 3% CEM energy

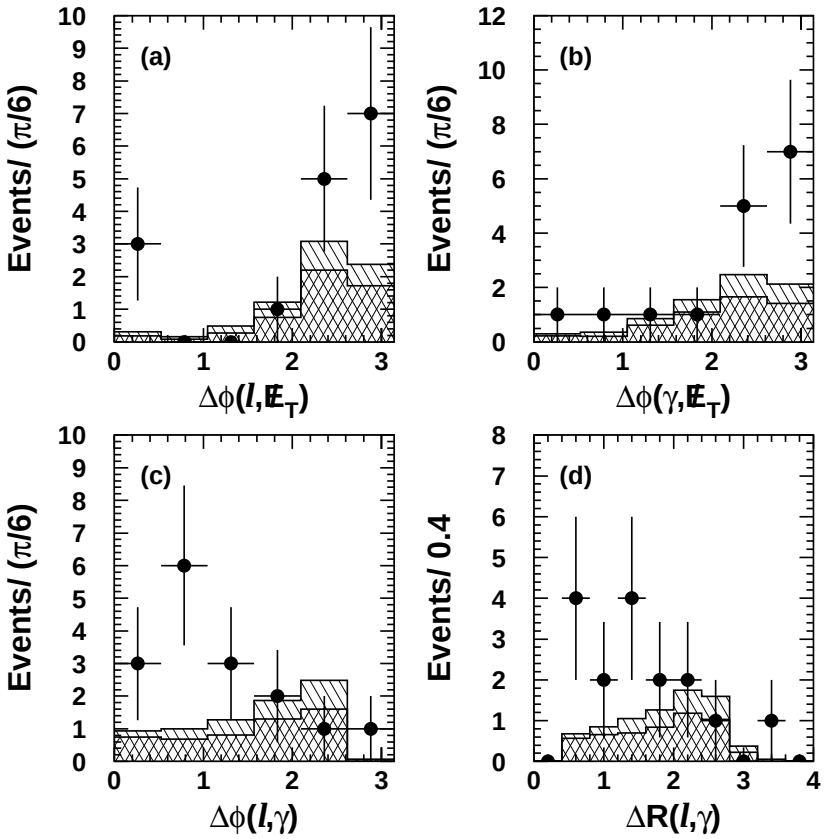

FIG. 18: The distributions for (a) $\Delta\varphi(\ell \not\!\!E_T)$, (b) $\Delta\varphi(\gamma \not\!\!E_T)$, (c) $\Delta\varphi_{\ell\gamma}$, and (d) $\Delta R_{\ell\gamma}$ in multibody $\ell\gamma \not\!\!E_T$ events. The points are CDF data, the hatched histogram is the total predicted mean background, and the cross-hatched histogram is the predicted mean diboson background.

resolution [14]. The masses of combinations of objects in observed $\ell\gamma \not\!\!E_T$ events are characterized by photon-lepton mass less than 100 GeV/c^2, lepton-$\not\!\!E_T$ transverse mass greater than 50 GeV/c^2, photon-$\not\!\!E_T$ transverse mass between 80 and 100 GeV/c^2, and $\ell\gamma \not\!\!E_T$ transverse mass between 90 and 120 GeV/c^2. The observed angular distributions favor smaller azimuthal photon-lepton separation and larger lepton-$\not\!\!E_T$ and photon-$\not\!\!E_T$ azimuthal separations than expected from the standard model. The difference in observed and predicted totals is therefore difficult to attribute to misidentified photons or leptons, which as shown in Figure 18 tend to have the larger photon-lepton azimuthal separation that is characteristic

Process	$e\gamma\not\!\!E_T X$	$\mu\gamma\not\!\!E_T X$	$\ell\gamma\not\!\!E_T X$
W+γ	1.9 ± 0.3	2.0 ± 0.3	3.9 ± 0.5
Z+γ	0.3 ± 0.1	1.0 ± 0.2	1.3 ± 0.2
ℓ+jet, jet $\to \gamma$	1.1 ± 0.2	1.0 ± 0.2	2.1 ± 0.4
$Z \to ee, e \to \gamma$	0.10 ± 0.04	-	0.10 ± 0.04
Hadron+γ	-	0.2 ± 0.1	0.2 ± 0.1
π/K Decay+γ	-	0.1 ± 0.1	0.1 ± 0.1
b/c Decay+γ	< 0.01	< 0.01	< 0.01
Predicted μ_{SM}	3.4 ± 0.3	4.2 ± 0.5	7.6 ± 0.7
Observed N_0	5	11	16
$P(N \geq N_0 \mid \mu_{SM})$	0.26	0.0054	0.0072

TABLE XVII: The mean number μ_{SM} of multi-body $\ell\gamma\not\!\!E_T$ events predicted by the standard model, the number N_0 observed in CDF data, and the observation likelihood $P(N \geq N_0|\mu_{SM})$. There exist correlated uncertainties between the different photon-lepton sources.

of a two-body final state.

C. Events with Additional Leptons or Photons

Process	$ee\gamma X$	$\mu\mu\gamma X$	$\ell\ell\gamma X$	$e\mu\gamma X$
Z+γ	3.3 ± 0.4	2.2 ± 0.3	5.5 ± 0.6	0.05 ± 0.01
ℓ+jet, jet $\to \gamma$	0.19 ± 0.04	0.13 ± 0.03	0.32 ± 0.07	—
Predicted μ_{SM}	3.5 ± 0.4	2.3 ± 0.3	5.8 ± 0.6	0.05 ± 0.01
Observed N_0	4	1	5	0
$P(N \geq N_0 \mid \mu_{SM})$	0.45	0.90	0.68	0.95

TABLE XVIII: The mean number μ_{SM} of multi-body events with additional leptons or photons predicted by the standard model, the number N_0 observed in CDF data, and the observation likelihood $P(N \geq N_0|\mu_{SM})$. There exist correlated uncertainties between the different photon-lepton sources.

The predicted and observed totals for multi-body multi-lepton events are compared in Table XVIII. Nearly all of the predicted total is expected from $Z^0\gamma$ production. Approxi-

Process	$e\gamma\gamma$	$\mu\gamma\gamma$	$\ell\gamma\gamma$
Z+γ	0.012 ± 0.012	0.004 ± 0.004	0.016 ± 0.016
ℓ+jet, jet $\to \gamma$	—	—	—
Predicted μ_{SM}	0.012 ± 0.012	0.004 ± 0.004	0.016 ± 0.016
Observed N_0	1	0	1
$P(N \geq N_0 \mid \mu_{SM})$	0.013	1.0	0.015

TABLE XIX: The mean number μ_{SM} of multi-body events with additional photons predicted by the standard model, the number N_0 observed in CDF data, and the observation likelihood $P(N \geq N_0|\mu_{SM})$. Expected contributions from jets misidentified as photons are negligible.

mately 6 events are expected; 5 events are observed, including the $ee\gamma\gamma\not\!\!E_T$ event. Both the electron and muon channels are in good agreement with the standard model. No $e\mu\gamma$ events were expected, and none were observed.

The predicted and observed totals for multi-body multi-photon events are compared in Table XIX. Only a small (0.01 event) contribution is expected from $Z\gamma$ production; the single event observed is the $ee\gamma\gamma\not\!\!E_T$ event. Judged solely as an event with one lepton with $E_T > 25$ GeV and two photons with $E_T > 25$ GeV, the observation likelihood of this event is 1.5%. Judged as an event with an additional lepton and large $\not\!\!E_T$, the observation likelihood is much smaller, as described in a previous analysis [3].

VI. CONCLUSION

We have performed an inclusive study of events containing at least one photon and one lepton (e or μ) in proton-antiproton collisions, motivated by the possibility of uncovering heretofore unobserved physical processes at the highest collision energies. In particular, the unexplained $ee\gamma\gamma\not\!\!E_T$ event, uncovered early on in the CDF analysis of the 1994-5 run of the Fermilab Tevatron, indicated that the samples of previously unexamined particle

combinations involving leptons and photons could contain potentially related, and therefore possibly novel, processes. The definition of the photon-lepton samples studied was chosen *a priori*, including the kinematic range of particles analyzed and the particle identification techniques employed. Wherever possible, the methods of previously published studies of leptons or photons at large transverse momentum were adopted. The questions of interest were also defined *a priori*, namely whether the event totals of the photon-lepton subsamples enumerated in Figure 3 agree with standard model predictions. As a supplemental result, the distributions of the kinematic properties of the various photon-lepton subsamples are presented in Section V.

The answers to those questions are as follows. A two-body photon-lepton sample, meant to encompass physical processes with two energetic particles in the final state, was observed to have a total (33 events) consistent with that of standard model predictions (25 events). Specifically, the observed total was greater then the predicted mean total, but the observation likelihood within the standard model of a total greater than or equal to that observed was more than 9%. A multi-body photon-lepton sample, meant to encompass physical processes with three or more energetic particles in the final state, was also observed to have an inclusive total (27 events) consistent with standard model predictions (20 events). The observed total was again higher than the predicted mean total, but the likelihood of a total greater than or equal to that observed was 10%.

Several subsets of the multi-body photon-lepton sample were studied for the presence of additional particles. A subset of multi-body photon-lepton events with additional leptons (5 $ee\gamma$ or $\mu\mu\gamma$ events and 0 $e\mu\gamma$ events) was observed to have good agreement with standard model predictions (6 events and 0 events, respectively). A subset of multi-body photon-lepton events with additional photons was studied, yielding only the unexplained $ee\gamma\gamma\not\!\!E_T$

event, whereas the predicted mean total of inclusive $\ell\gamma\gamma$ events (requiring the presence of neither $\not\!\!E_T$ nor a second lepton) is 0.01, an observation likelihood of 1%. This event and estimations of its likelihood have been analyzed elsewhere [3].

Finally, a subset of the multi-body photon-lepton sample, consisting of those events with $\not\!\!E_T > 25$ GeV, was observed to have a total (16 events) that is substantially greater than that predicted by the standard model (7.6 ± 0.7 events). The likelihood of a total greater than or equal to that observed was 0.7%. Moreover, the excess events in the observed inclusive multi-body photon-lepton sample can be completely accounted for by the excess in the multi-body $\ell\gamma\not\!\!E_T$ sample; observed multi-body photon-lepton events with $\not\!\!E_T < 25$ GeV agree well with the standard model.

Category	μ_{SM}	N_0	$P(N \geq N_0 \mid \mu_{SM})$ %
All $\ell\gamma X$	—	77	—
Z-like $e\gamma$	—	17	—
Two-Body $\ell\gamma X$	24.9 ± 2.4	33	9.3
Multi-Body $\ell\gamma X$	20.2 ± 1.7	27	10.0
Multi-Body $\ell\ell\gamma X$	5.8 ± 0.6	5	68.0
Multi-Body $\ell\gamma\gamma X$	0.02 ± 0.02	1	1.5
Multi-Body $\ell\gamma\not\!\!E_T X$	7.6 ± 0.7	16	0.7

TABLE XX: The results for all photon-lepton categories analyzed, including the mean number of events μ_{SM} predicted by the standard model, the number N_0 observed in CDF data, and the observation likelihood $P(N \geq N_0 \mid \mu_{SM})$.

That the standard model prediction yields the observed total of a particular sample of events with 0.7% likelihood (equivalent to 2.7 standard deviations for a Gaussian distribution) is an interesting result, but it is not a compelling observation of new physics. Multi-purpose particle physics experiments analyze dozens of independent samples of events, making a variety of comparisons with the standard model for each sample. In the context of this

analysis alone, five mostly independent subsamples of photon-lepton events were analyzed. This large number of independent comparisons with the standard model for the same collection of data increases the chance that outcomes with $\sim 1\%$ likelihood occur. However, once a particular comparison has been identified as anomalous, the same comparison performed with subsequent experiments is no longer subject to the dilution of its significance by the number of other independent comparisons performed concurrently. Hence an observation of increased significance in the forthcoming run of the Fermilab Tevatron would confirm decisively the failure of the standard model to describe $\ell\gamma\not\!\!E_T$ production; an observation of no significant excess would confirm the present result as a statistical fluctuation.

Acknowledgments

We thank the Fermilab staff and the technical staffs of the participating institutions for their vital contributions. We thank U. Baur and S. Mrenna for their prompt response to our need for programs to calculate the standard model $W\gamma$ and $Z\gamma$ backgrounds used in this analysis. This work was supported by the U.S. Department of Energy and National Science Foundation; the Italian Istituto Nazionale di Fisica Nucleare; the Ministry of Education, Culture, Sports, Science, and Technology of Japan; the Natural Sciences and Engineering Research Council of Canada; the National Science Council of the Republic of China; the Swiss National Science Foundation; the A. P. Sloan Foundation; the Bundesministerium fuer Bildung und Forschung, Germany; the Korea Science and Engineering Foundation (KoSEF); the Korea Research Foundation; and the Comision Interministerial de Ciencia y Tecnologia,

Spain.

---

[1] S. L. Glashow, Nucl. Phys. **22** 588, (1961); S. Weinberg, Phys. Rev. Lett. **19** 1264, (1967); A. Salam, Proc. 8th Nobel Symposium, Stockholm, (1979).

[2] F. Abe *et al.*, Nucl. Instrum. Methods Phys. Res., Sect. A **271**, 387 (1988). The CDF coordinate system defines r, φ, and z as cylindrical coordinates, with the z-axis along the direction of the proton beam. The angle θ is the polar angle relative to the z-axis, the pseudorapidity is defined as $\eta = -\ln(\tan(\theta/2))$, and the transverse energy is defined as $E_T = E\sin\theta$. Missing transverse energy ($\not\!\!E_T$) is the vector opposite to the vector sum of the transverse energies of all objects in an event, $\not\!\!E_T = -\Sigma E_T$.

[3] F. Abe *et al.*, Phys. Rev. D **59**, 092002 (1999). The PEM electron candidate, while satisfying all standard selection criteria, is found to have tracking data inconsistent with that of control samples, as described in these references.

[4] S. Ambrosanio, G. L. Kane, G. D. Kribs, S. P. Martin, and S. Mrenna, Phys. Rev. Lett. **76**, 3498 (1996); G. L. Kane and S. Mrenna, Phys. Rev. Lett. **77** 3502 (1996); S. Ambrosanio, G. L. Kane, G. D. Kribs, S. P. Martin, and S. Mrenna, Phys. Rev. D **55**, 1372 (1997).

[5] R. Barate *et al.*, Eur. Phys. J. C **16** 71, (2000); B. Abbott *et al.*, Phys. Rev. Lett. **82**, 2244 (1999); B. Abbott *et al.*, Phys. Rev. Lett. **80**, 442 (1998); B. Abbott *et al.*, Phys. Rev. Lett. **81**, 524 (1998); F. Abe *et al.*, Phys. Rev. Lett **81**, 1791 (1998); P. J. Wilson, in *ICHEP 98*, Proceedings of the 29th International Conference in High-energy Physics, Vancouver, Canada, 1998, edited by A. Astbury, D. Axen and J. Robinson (World Scientific, Singapore, 1998); S. Abachi *et al.*, Phys. Rev. Lett. **78**, 2070 (1997); P.D. Acton *et al.*, Phys. Lett. **B311** 391, (1993).

[6] B. Abbott *et al.*, Phys. Rev. Lett. **82**, 29 (1999).

[7] F. Abe *et al.*, Phys. Rev. Lett **83**, 3124 (1999).

[8] F. Snider *et al.*, Nucl. Instrum. Methods **A268**, 75 (1988). This is the reference for the previous generation of the device. The replacement for the 1994-5 data sample has more modules, each with a shorter drift length but is otherwise similar.

[9] F. Abe *et al.*, Phys. Rev. D **59**, 052002 (1999).

[10] G. W. Foster *et al.*, Nucl. Instrum. Methods Phys. Res. A **268**, 33 (1988).

[11] T. Affolder *et al.*, Phys. Rev. D **63**, 032003 (2001); F. Abe *et al.*, Phys. Rev. D **50**, 2966 (1994).

[12] T. Affolder *et al.*, Phys. Rev. D **64**, 052001 (2001); F. Abe *et al.*, Phys. Rev. D **52**, 4784 (1995).

[13] Trigger towers subtend 0.2 in η by 15° in φ.

[14] J. Berryhill, Ph.D. thesis, University of Chicago, 2000.

[15] M. Kruse, Ph.D. thesis, Purdue University, 1996.

[16] J. Wahl, Ph. D. thesis, University of Chicago, 1999; F. Abe *et al.*, Phys. Rev. D **52**, 2624 (1995).

[17] F. Abe *et al.*, Phys. Rev. D **45**, 1448 (1992).

[18] U. Baur and S. Mrenna, private communication. The source code is available publicly at `http://moose.ucdavis.edu/mrenna/code/`.

[19] U. Baur and E. L. Berger, Phys. Rev. D **47**, 4889 (1993); **41**, 1476 (1990).

[20] T. Sjostrand, Computer Physics Commun. **82** (1994) 74; S. Mrenna, Computer Physics Commun. **101** (1997) 232. An archive of program versions and documentation is available publicly at `http://www.thep.lu.se/tf2/staff/torbjorn/Pythia.html`.

[21] H. L. Lai *et al.*, Eur. Phys. J. C **12**, 375 (2000). The source code is available publicly at `http://www.phys.psu.edu/~cteq/CTEQ5Table/`.

[22] TAUOLA version 2.5 (June 1994), S. Jadach *et al.*, Computer Phys. Commun. **76** 361 (1993).

[23] A.D. Martin, R.G. Roberts, W.J. Stirling, and R.S. Thorne, Eur. Phys. J. C **4**, 463 (1998). A 5% uncertainty is recommended for W and Z^0 boson production at the Tevatron. The parton species and momenta contributing to $W\gamma$ and $Z^0\gamma$ production are very similar.

[24] U. Baur, T. Han, and J. Ohnemus, Phys. Rev. D **57** (1998) 2823; U. Baur, T. Han, and J. Ohnemus, Phys. Rev. D **48** (1993) 5140; J. Ohnemus, Phys. Rev. D **47** (1993) 940.

[25] D. Cronin-Hennessy *et al.*, Nucl. Instrum. Methods Phys. Res., Sect. A **443/1**, 37-50 (2000).

[26] D.E. Groom *et al.*, Eur. Phys. J. C **15**, 1 (2000). Computer-readable data files may be found at `http://pdg.lbl.gov/xsect/contents.html`.

[27] D. Buskulic *et al.*, Z. Phys. **C66**, 355 (1995); P. Abreu *et al.*, Nucl. Phys. **B444**, 3 (1995); R. Akers *et al.*, Z. Phys. **C63**, 181 (1994); H. Aihara *et al.*, Phys. Rev. Lett. **61**, 1263 (1988); D. Antreasyan *et al.*, Phys. Rev. Lett. **38**, 115 (1977); J.W. Cronin *et al.*, Phys. Rev. **D11**, 3105 (1975).

[28] QQ version 8.08 (June 1991), P. Avery, K. Read, G. Trahern, Cornell Inernal Report No. CSN-212 (1985), unpublished.

[29] S. Kuhlmann, Report No. FERMILAB-CONF-99-165-E (1998); F. Abe *et al.*, Phys. Rev. D **60**, 092003 (1999); Phys. Rev. Lett. **77**, 5005 (1996).